

UNIVERSIDADE ESTADUAL DE MARINGÁ
TECHNOLOGY CENTER
DEPARTMENT OF CIVIL ENGINEERING
GRADUATE PROGRAM IN CIVIL ENGINEERING
- Master of Science

JULIANA SANTOS WAGNER

**A COMPARATIVE ANALYSIS BETWEEN 3D-PRINTED AND MOLD-CAST
CEMENTITIOUS MORTAR: physical, mechanical, and microstructural properties**

**ANÁLISE COMPARATIVA ENTRE ARGAMASSA CIMENTÍCIA IMPRESSA EM
3D E MOLDADA: propriedades físicas, mecânicas e microestruturais**

MARINGÁ
2023

JULIANA SANTOS WAGNER

**A COMPARATIVE ANALYSIS BETWEEN 3D-PRINTED AND MOLD-CAST
CEMENTITIOUS MORTAR: physical, mechanical, and microstructural properties**

**ANÁLISE COMPARATIVA ENTRE ARGAMASSA CIMENTÍCIA IMPRESSA EM
3D E MOLDADA: propriedades físicas, mecânicas e microestruturais**

Master's thesis presented as part of the necessary requirements for obtaining the title of Master of Science in Civil Engineering from the Graduate Program in Civil Engineering at the State University of Maringá.

Supervisor: Dr. Romel Dias Vanderlei

Co-supervisor: Dr. Sreekanta Das

MARINGÁ
2023

Dados Internacionais de Catalogação-na-Publicação (CIP)
(Biblioteca Central - UEM, Maringá - PR, Brasil)

W132c

Wagner, Juliana Santos

A comparative analysis between 3d-printed and mold-cast cementitious mortar : physical, mechanical, and microstructural properties / Juliana Santos Wagner. -- Maringá, PR, 2023.

64 f.: il. color., figs., tabs.

Orientador: Prof. Dr. Romel Dias Vanderlei.

Coorientador: Prof. Dr. Sreekanta Das.

Dissertação (Mestrado) - Universidade Estadual de Maringá, Centro de Tecnologia, Departamento de Engenharia Civil, Programa de Pós-Graduação em Engenharia Civil, 2023.

1. Argamassa cimentícia - Impressão 3D. 2. Anisotropia. 3. Resistência de ligação. 4. Construção civil. 5. Construção - Tecnologia. I. Vanderlei, Romel Dias, orient. II. Das, Sreekanta, coorient. III. Universidade Estadual de Maringá. Centro de Tecnologia. Departamento de Engenharia Civil. Programa de Pós-Graduação em Engenharia Civil. IV. Título.

CDD 23.ed. 624.1833

Elaine Cristina Soares Lira - CRB-9/1202

JULIANA SANTOS WAGNER

A COMPARATIVE ANALYSIS BETWEEN 3D-PRINTED AND MOLD-CAST CEMENTITIOUS MORTAR: PHYSICAL, MECHANICAL, AND MICROSTRUCTURAL PROPERTIES

ANÁLISE COMPARATIVA ENTRE ARGAMASSA CIMENTÍCIA IMPRESSA EM 3D E MOLDADA: PROPRIEDADES FÍSICAS, MECÂNICAS E MICROESTRUTURAS

Master's thesis presented on 25/07/2023, deemed suitable for the attainment of the degree of MASTER OF SCIENCE IN CIVIL ENGINEERING, and approved in its final form, as a partial requirement for the attainment of the degree of MASTER OF SCIENCE IN CIVIL ENGINEERING from the STATE UNIVERSITY OF MARINGÁ

EXAMINATION BOARD



Dr. Romel Dias Vanderlei
Graduate Program in Civil Engineering
State University of Maringá
Supervisor



Dr. Luís Antônio Guimarães Bitencourt Júnior
Graduate Program in Civil Engineering
Polytechnic School of the University of São Paulo



Dr. Paulo Ricardo de Matos
Graduate Program in Civil Engineering
University of the State of Santa Catarina

JULIANA SANTOS WAGNER

A COMPARATIVE ANALYSIS BETWEEN 3D-PRINTED AND MOLD-CAST CEMENTITIOUS MORTAR: PHYSICAL, MECHANICAL, AND MICROSTRUCTURAL PROPERTIES

ANÁLISE COMPARATIVA ENTRE ARGAMASSA CIMENTÍCIA IMPRESSA EM 3D E MOLDADA: PROPRIEDADES FÍSICAS, MECÂNICAS E MICROESTRUTURAS

Dissertação de Mestrado apresentada no dia 25/07/2023, julgada adequada para a obtenção do título de MESTRA EM ENGENHARIA CIVIL e aprovada em sua forma final, como requisito parcial para a obtenção do título de MESTRA EM ENGENHARIA CIVIL DA UNIVERSIDADE ESTADUAL DE MARINGÁ

BANCA EXAMINADORA


Prof. Dr. Romel Dias Vanderlei

Programa de Pós-Graduação em Engenharia Civil
Universidade Estadual de Maringá
Professor Orientador



Prof. Dr. Luís Antônio Guimarães Bitencourt Júnior
Programa de Pós-Graduação em Engenharia Civil
Escola Politécnica da Universidade de São Paulo



Prof. Dr. Paulo Ricardo de Matos
Programa de Pós-Graduação em Engenharia Civil
Universidade do Estado de Santa Catarina

I dedicate this work to my family, who have always supported me, and to my partner, Marcos Silveira, for choosing to accompany me on this journey.

ACKNOWLEDGMENTS

To the Emerging Leaders in the Americas Program (ELAP) for providing Mrs. Juliana Santos Wagner with a scholarship for this research.

This study was financed in part by the Coordenação de Aperfeiçoamento de Pessoal de Nível Superior - Brasil (CAPES) - Finance Code 001.

To the Canada Mortgage and Housing Corporation (CMHC) for the generous support of this research project.

To the Natural Sciences and Engineering Research Council of Canada (NSERC) for their partial funding of this study.

To Dr. Romel Dias Vanderlei from the Universidade Estadual de Maringá and Dr. Sreekanta Das from the University of Windsor for the orientation and support.

To Dr. Luís Antonio Guimarães Bitencourt Júnior, Dr. Oscar Aurelio Mendoza Reales, and Dr. Paulo Ricardo de Matos for their invaluable contributions to this research project.

To the technical staff members of the University of Windsor Structural Engineering Laboratory, Mr. Matthew St. Louis, and Mr. Jerome Finnerty, for their invaluable assistance throughout the course of this research project.

To Ms. Fiona Coughlin and Mrs. Pamela Breault from Habitat for Humanity Windsor-Essex, for advocating for women in engineering, construction, and business.

To the students of the 3DCP research group of the University of Windsor, Mr. Marcos V. G. Silveira, Mr. Mohsen Khanverdi, and Mr. Siddharth Popli.

Doing the best at this moment puts you
in the best place for the next moment.

Oprah Winfrey

ABSTRACT

The application of 3D printing in construction requires the standardization of testing procedures specifically designed for this technology. This paper investigates the material properties of a 3D-printable cementitious mortar and provides a comparative analysis of the physical, mechanical, and microstructural behavior between 3D-printed and mold-cast specimens. The anisotropy of 3D-printed specimens under various loading scenarios and directions was evaluated using Analysis of Variance. Furthermore, the Digital Image Correlation (DIC) technique was employed to examine the strain behavior and generate stress-strain curves for 3D-printed structures under compressive strength. The results indicated a significant strength reduction for the 3D-printed specimens across all mechanical tests, and the DIC revealed strain propagation within the interlayers of the 3D-printed specimens. Finally, the oblique shear test was considered a viable option for evaluating the shear strength of 3D-printed structures, while the four-point flexural strength test was recommended as the preferred method for assessing interlayer bond strength.

Keywords: 3D-printed cementitious mortar. Anisotropy. Interlayer bond strength.

RESUMO

A aplicação da impressão 3D na construção requer a padronização de testes especificamente projetados para essa tecnologia. Este artigo investiga as propriedades materiais de uma argamassa cimentícia para impressão 3D e fornece uma análise comparativa do comportamento físico, mecânico e microestrutural entre espécimes impressas em 3D e moldadas. A anisotropia das espécimes impressas em 3D sob diferentes cenários e direções de carregamento foi avaliada usando Análise de Variância. Além disso, a técnica de Correlação de Imagem Digital (DIC) foi empregada para examinar o comportamento da deformação e gerar curvas de tensão-deformação para estruturas impressas em 3D sob compressão. Os resultados indicaram uma redução significativa na resistência das espécimes impressas em 3D em todos os testes mecânicos, e a DIC revelou a propagação da deformação entre as camadas das espécimes impressas em 3D. Por fim, o teste de cisalhamento oblíquo foi considerado uma opção viável para avaliar a resistência ao cisalhamento de estruturas impressas em 3D, enquanto o teste de resistência à flexão de quatro pontos foi recomendado como o método preferido para avaliar a resistência de ligação entre camadas.

Palavras-chave: Argamassa cimentícia impressa em 3D. Anisotropia. Resistência de ligação entre camadas.

LIST OF FIGURES

Figure 4.1 – Oblique shear test. a) illustration; b) test setup	21
Figure 4.2 – Pore morphology and location. a) spherical pores of mold-cast specimens; b) irregular shaped pores of 3D-printed specimens; with higher porosity in the interlayer; c) pore distribution in mold-cast specimens; d) pore distribution in 3D-printed specimens, with higher porosity in the interlayers	22
Figure 4.3 – Mechanical tests setup. a) compressive strength; b) splitting tensile strength; c) four-point flexural strength.....	24
Figure 4.4 – Tensile strength tests. a) splitting tensile; b) direct tensile	26
Figure 5.1 – Printing set up. a) robotic arm; b) similar pump used for printing	29
Figure 5.2 – 3D-printed wall design. a) floor plan; b) section; c) 3D view	30
Figure 5.3 – 3D-printed walls. a) first day of printing; b) second day of printing	31
Figure 5.4 – Mold-cast specimens	33
Figure 5.5 – Mechanical tests and load direction	34
Figure 5.6 – Testing process. a) capping of 3D-printed specimens for loading in the Y-direction; b) speckle pattern made on the front surface of the specimens; c) mechanical test setup.....	35
Figure 5.7 – Samples for PSD and XRF analyses	36
Figure 5.8 – SEM and EDS analyses. a) environmental FEI Quanta 200 FEG; b) samples attached to the stage.....	42
Figure 6.1 – Cumulative percent passed vs. sieve opening curve	43
Figure 6.2 – Fibers found during the sieve analysis of fine and coarse aggregates, ruler for scale, in inches.....	44
Figure 6.3 – Volume over vs. particle size curve	44
Figure 6.4 – UPV vs. compressive strength graphic.....	47
Figure 6.5 - DIC analysis of the 3D-printed specimens under compressive strength. a) principal major strain of cubes tested in X-direction; b) principal minor strain of cubes tested in X-direction; c) principal major strain of cubes tested in Z-direction; d) principal minor strain of cubes tested in Z-direction.....	49
Figure 6.6 – Stress vs. strain curves.....	50
Figure 6.7 - DIC analysis of the 3D-printed specimens under oblique shear strength. a) principal major strain of cubes tested in X-direction; b) principal minor strain of cubes tested in X-direction; c) principal major strain of cubes tested in Z-direction; d) principal minor strain of cubes tested in Z-direction.....	51

Figure 6.8 - DIC analysis of the 3D-printed specimens under splitting tensile strength. a) principal major strain of cubes tested in X-direction; b) principal minor strain of cubes tested in X-direction; c) principal major strain of cubes tested in Z-direction; d) principal minor strain of cubes tested in Z-direction	52
Figure 6.9 - DIC analysis of the 3D-printed specimens under flexural strength. a) three-point flexural test, principal major strain of prisms tested in X-direction; b) four-point flexural test, principal major strain of prisms tested in X-direction.....	53
Figure 6.10 – Pore morphology. a) mold-cast sample at magnitude 35x; b) 3D-printed sample in XY plane at magnitude 35x; c) 3D-printed sample in YZ plane at magnitude 30x.....	54
Figure 6.11 – SEM and EDS analyses on the fibers. a) fiber diameters recorded at magnitude 1500x; b) overlay of elements at magnitude 110x	55
Figure 6.12 – SEM analysis on the interlayer at YZ plane. a) Visible portion of the interlayer at the edge of the 3D-printed sample, at magnitude 30x; b) Widths recorded at the visible portion of the interlayer, at magnitude 1500x.....	55

LIST OF TABLES

Table 5.1 – Printing parameters.....	30
Table 5.2 – Hydraulic cement mortar flow tests results	32
Table 5.3 – Performed tests	34
Table 6.1 – Chemical composition of the dry premixed mortar.....	45
Table 6.2 – Results from the physical tests	46
Table 6.3 – Results of mechanical tests.....	48
Table 6.4 – Compressive strength results obtained from the stress vs. strain curves.....	50

LIST OF SYMBOLS

CAPITAL ROMAN LETTERS

A	Mass of oven-dried sample in air
A_f	Fracture area of the specimens
A_s	Area of loaded surface
C	Mass of surface-dry sample in air after immersion and boiling
D	Apparent mass of sample in water after immersion and boiling
L	Span length
L_t	Distance between centers of transducer faces
P	Maximum applied load
R	Flexural strength
S	Rate of increase in the maximum stress on the tension face
T	Splitting tensile strength
T_t	Transit time
V	Pulse velocity

LOWERCASE ROMAN LETTERS

a	Average distance between the line of fracture and the nearest support measured on the tension surface of the beam
b	Average width of the specimen
c	Cross-section of the specimen
d	Average depth of the specimen
f_m	Compressive strength
l	Length of the line of contact with the specimen
p	Significance level
r	Loading rate

GREEK LETTERS

α	Inclination angle of the specimen
τ	Shear strength

ABBREVIATIONS

3DCP	3D concrete printing
AM	Additive manufacturing
ANOVA	Analysis of variance
ASTM	American Society for Testing and Materials
COV	Coefficient of variance
DIC	Digital image correlation
EDS	Energy-dispersive x-ray spectroscopy
ISO	International Organization for Standardization
PSD	Particle size distribution
SEM	Scanning electron microscopy
STL	Standard Triangulation
UPV	Ultrasonic pulse velocity
XRF	X-ray fluorescence

SUMMARY

1. INTRODUCTION	15
2. JUSTIFICATION	17
3. GOALS	18
3.1. Main goal	18
3.2. Specific goals	18
4. LITERATURE REVIEW	19
4.1. Related research	20
5. EXPERIMENTAL PROGRAM	29
5.1. 3D specimen preparation.....	29
5.2. Mold-cast specimen preparation	31
5.3. Test Matrix	33
5.3.1. Sieve analysis of fine and coarse aggregates	35
5.3.2. Particle size distribution (PSD) and x-ray fluorescence (XRF)	36
5.3.3. Density, absorption, and voids	36
5.3.4. Ultrasonic pulse velocity (UPV).....	37
5.3.5. Compressive strength	38
5.3.6. Oblique shear strength	38
5.3.7. Splitting tensile strength.....	39
5.3.8. Three-point flexural strength.....	39
5.3.9. Four-point flexural strength.....	40
5.3.10. Scanning electron microscope (SEM) and energy-dispersive x-ray spectroscopy (EDS)	42
6. RESULTS AND DISCUSSION	43
6.1. Material tests	43
6.2. Physical tests	45
6.3. Mechanical tests	47
6.3.1. Compressive strength	48
6.3.2. Oblique shear strength	50
6.3.3. Splitting tensile strength.....	51
6.3.4. Three and four-point flexural strengths	52
6.4. Microstructural tests	54
7. CONCLUSION	56
7.1. Recommendations	58
REFERENCES	59

1. INTRODUCTION

The construction industry has experienced stagnant productivity levels that have remained unchanged for over 80 years (SANJAYAN; NAZARI; NEMATOLLAHI, 2019), lagging significantly behind other industries such as automotive or aerospace (BUSWELL et al., 2007). This industry relies on manual labor, resulting in challenges such as low productivity and a shortage of skilled workers (MECHTCHERINE et al., 2019b). Sustainability concerns are also prevalent, as the construction sector is responsible for approximately 80% of worldwide waste. Most existing construction methods and materials are not sustainable (NEMATOLLAHI; XIA; SANJAYAN, 2017). For instance, concrete, the most widely utilized construction material globally, contributes up to 8% of global CO₂ emissions through cement manufacturing (ANDREW, 2018). Moreover, the usage of formwork constitutes approximately 80% of concrete construction costs worldwide and generates substantial waste when discarded (NEMATOLLAHI; XIA; SANJAYAN, 2017).

The concept of improving the processes of constructing concrete buildings was initially conceived by Thomas Edison in 1908 (EDISON, 1917). However, it was not until 1997 that a successful study on the efficacy of additive manufacturing (AM) in construction automation was conducted by Pegna (1997). AM involves adding or combining materials to fabricate three-dimensional objects (BUSWELL et al., 2007). Pegna (1997) proposed a methodology that involved the sequential deposition of a thin layer of sand, followed by a layer of cement, and the subsequent application of steam to expedite the curing process. This pioneering work laid the foundation for the emergence of 3D concrete printing (3DCP) as a promising solution for automating construction processes (SANJAYAN; NAZARI; NEMATOLLAHI, 2019). The White House recently recognized AM as a crucial and emerging technology (FAST TRACK ACTION SUBCOMMITTEE ON CRITICAL AND EMERGING TECHNOLOGIES, 2022). And the introduction of the new Unified Facilities Criteria has established specific requirements for 3D-printed concrete structures (DEPARTMENT OF DEFENSE, 2022). Furthermore, the ISO Technical Committee 261 of additive manufacturing released the ISO/ASTM DIS 52939, which states the qualification principles for structural and infrastructure elements (ISO/TC 261 ADDITIVE MANUFACTURING, 2022).

3DCP can be classified into five distinct approaches: (i) selective deposition by extrusion, (ii) selective application by spraying, (iii) selective binding, (iv) adaptive sliding formwork, and (v) reinforcement mesh as an integrated formwork (MECHTCHERINE et al.,

2019a). In this study, selective deposition by extrusion was utilized. The process begins with the creation of a 3D solid model using Computer-aided Design software, which is then converted into the Standard Triangulation (STL) format, commonly employed by rapid manufacturing machines. The STL format divides the surface of the object into layers that can be sequentially constructed. Consecutively, this information is transmitted to the machine, which deposits the material layer by layer using an extrusion printhead to fabricate the 3D object (BUSWELL et al., 2007; DAUNGWILAILUK; PHEINSUSOM; PANSUK, 2021). Alongside the printhead, the 3D printers feature a positioning system or manipulator responsible for moving the printhead and ensuring the supply of concrete through hoses or pipes (MECHTCHERINE et al., 2019a). Compared to traditional concrete construction methods, 3DCP technology offers numerous advantages. These include reduced dependence on manual labor, elimination of hazardous tasks, creation of technology-driven job opportunities, elimination of formwork usage, shortened construction timelines, enhanced architectural flexibility for complex designs, and precise material deposition that minimizes errors, resulting in superior interior and exterior finishes (BUSWELL et al., 2007; NEMATOLLAHI; XIA; SANJAYAN, 2017; SANJAYAN; NAZARI; NEMATOLLAHI, 2019).

This project was part of a collaboration between the State University of Maringá (Brazil) and the University of Windsor (Canada) through the Emerging Leaders in the Americas Program (ELAP) scholarship. The experimental program was carried out at the Structural Engineering Laboratory of the University of Windsor, Canada. The primary objective of this study was to investigate the physical, mechanical, and microstructural properties of 3D-printed specimens. Using a robotic arm and a mortar pump system, a wall was 3D-printed with a proprietary cementitious mortar. Subsequently, a series of cubic and prismatic were saw-cut from the 3D-printed wall and tested in various loading scenarios and directions. The results were compared with those of mold-cast specimens to ensure a reliable reference. Furthermore, a comprehensive analysis was conducted to assess the characteristics of the 3D-printable cementitious mortar.

2. JUSTIFICATION

The utilization of 3D printing for structural applications in construction creates a need for standardizing materials requirements, design solutions, and testing procedures that accurately assess the mechanical characteristics of 3DCP. Therefore, the present study investigated the material properties of a 3D-printable cementitious mortar. Additionally, 3D-printed specimens have been subjected to physical, mechanical, and microstructural tests. Various loading scenarios and directions have been investigated. A comparative analysis was performed using mold-cast specimens as referential. This research aims to promote discussion on appropriate testing procedures for evaluating the behavior of 3DCP. Moreover, the findings of this research have the potential to contribute to the development of numerical models able to assist the design of 3D-printed structures.

3. GOALS

3.1. Main goal

Explore the material properties of a 3D-printable cementitious mortar, and compare the physical, mechanical, and microstructural behavior between 3D-printed and mold-cast specimens.

3.2. Specific goals

- i. Analyse the anisotropic behavior of 3D-printed specimens under various loading scenarios and directions.
- ii. Explore the strain propagation in 3D-printed specimens using Digital Image Correlation (DIC).
- iii. Propose stress-strain equations for 3D-printed and mold-cast specimens under compression.
- iv. Evaluate the potential of the oblique shear test for assessing the shear strength of 3D-printed structures.
- v. Compare different test methods that assess the interlayer bond strength of 3D-printed specimens.

4. LITERATURE REVIEW

The rapid growth of 3DCP has raised pertinent concerns and prompted extensive research in various areas. State-of-the-art reviews were done by different authors (ADALOUDIS; BONNIN ROCA, 2021; CHEN et al., 2022a; HEIDARNEZHAD; ZHANG, 2022; KRUGER; ZIJL, 2021; MOHAN et al., 2021; NEMATOLLAHI; XIA; SANJAYAN, 2017; ROUSSEL, 2018; SOUZA et al., 2020; XIAO et al., 2021), and a comparative study between 3DCP and other construction methods, such as prefabricated modular construction, cast in situ reinforced concrete, cold-formed steel, and hot-rolled steel, was carried out by Batikha *et al.* (2022). Experimental works regarding the fresh properties of 3D-printed mortars can be found in diverse research papers. This includes the replacement of part of the cement for recycled powder (HOU et al., 2021), the effect of using recycled PET as a replacement for natural aggregates (SKIBICKI et al., 2022), the addition of retarders, accelerators, and superplasticizers to 3D-printed Portland cement (TRAMONTIN SOUZA et al., 2022), or the effect of recycled sand on plastic shrinkage and cracking of 3D-printed mortar (ZHANG; XIAO, 2021).

Some research explored the incorporation of polymeric or metallic fibers into 3DCP (FARINA et al., 2016; SINGH et al., 2022; TRAN; CU; LE, 2021) and 3D printing ultra-high-performance fiber-reinforced concrete (YANG et al., 2022a, 2022b). Solutions for the reinforcement of the interlayer bond strength were studied with the insertion of metal or steel cables, U-shaped nails, carbon fiber-reinforced polymer grids, and barbed wire during the printing (BOS et al., 2017; HOJATI et al., 2022; SUN et al., 2022; WANG et al., 2021; XIAO et al., 2022). Alternatives included the addition of bonding agents between layers, such as sulfur-black carbon sand mortar, cement strengthener, polymer solution, or cement paste (HOSSEINI et al., 2019; WENG et al., 2021).

Research papers regarding the tests of large-scale 3DCP include unconfined uniaxial load or axial compression load tests on walls (DAUNGWILAILUK; PHEINSUSOM; PANSUK, 2021; HAN et al., 2022), four-point bending tests on beams with different types of interlayer shear and longitudinal reinforcement (GEBHARD et al., 2021), the structural performance of a post-tensioned concrete girder designed by topology optimization (VANTYGHM et al., 2020), the evaluation of geometric quality assurance of 3D concrete printed and hybrid construction elements (BUSWELL et al., 2022), and the 3D printing of ultra-high-performance concrete wall elements with a new additive manufacturing processing route

(GOSSELIN et al., 2016).

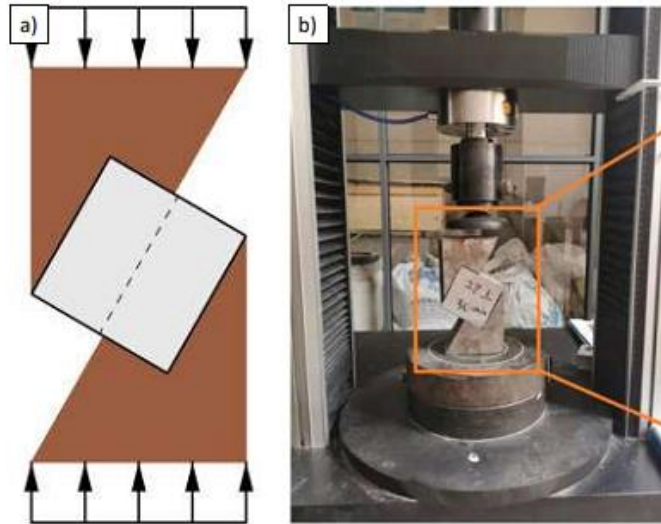
Analytical, constitutive, and numerical models of 3D-printed concrete were proposed by diverse authors. Some of their purposes included the prediction of the buckling failure of a 3DCP cylinder under its dead weight (LIU; SUN, 2021), the estimation of the surface moisture and prediction of the lack of interlayer adhesion (MOELICH; KRUGER; COMBRINCK, 2021), the simulation of elastic buckling and plastic collapse failure mechanisms (NGUYEN-VAN et al., 2022), the simulation of extrusion process and prediction of layer shape during 3DCP (REINOLD et al., 2022), the prediction of structural capacity and failure mechanisms of reinforced concrete deep beams under various loading configurations (VAN DEN HEEVER et al., 2022a), the prediction of the mechanical response of the interface of 3DCP under shear stress (WANG et al., 2022), and the simulation of the anisotropic mechanical behavior of 3DCP under compression and flexure (XIAO; LIU; DING, 2021). Research papers on the hardened properties of 3D-printed specimens are described below. These studies have similarities with the work in hand and provided valuable insights into comprehending the testing procedures employed in this research.

4.1. Related research

Mechtcherine *et al.* (2022) presented a comprehensive guide for evaluating the hardened properties of cement-based materials produced using AM. Their review primarily focused on the mechanical properties of materials with a layered structure, which exhibit significant anisotropy compared to traditional cast concrete. The authors emphasized the importance of testing the mechanical properties of 3D-printed specimens in various directions relative to the printing path and considering these results on structural design requirements. Among the different recommended tests investigating the properties of 3DCP, the following are included in the present research paper: density, compressive strength, tensile/flexural strength, and interlayer bond strength. The authors also highlighted the need for specific specimen geometries when extracting samples from 3DCP elements, as traditional concrete codes often demand larger specimen sizes that may not align with the layer size constraints. Therefore, it is common to employ geometries required by mortar codes when testing 3DCP. Mechtcherine *et al.* (2022) acknowledge the limitation of the splitting tensile test when characterizing the anisotropic behavior of 3D-printed specimens. This limitation occurs because the fracture plane is defined by the test setup, meaning that the results depend on the location of the interlayer relative to the

applied force vector. Additionally, the authors recommended using the four-point flexural strength test to assess the flexural tensile strength of 3D-printed specimens. Finally, among various tests to investigate the shear bond strength of 3D-printed elements, illustrated in Figure 4.1, the authors suggested the oblique shear strength test proposed by Xu *et al.* (2021).

Figure 4.1 – Oblique shear test. a) illustration; b) test setup



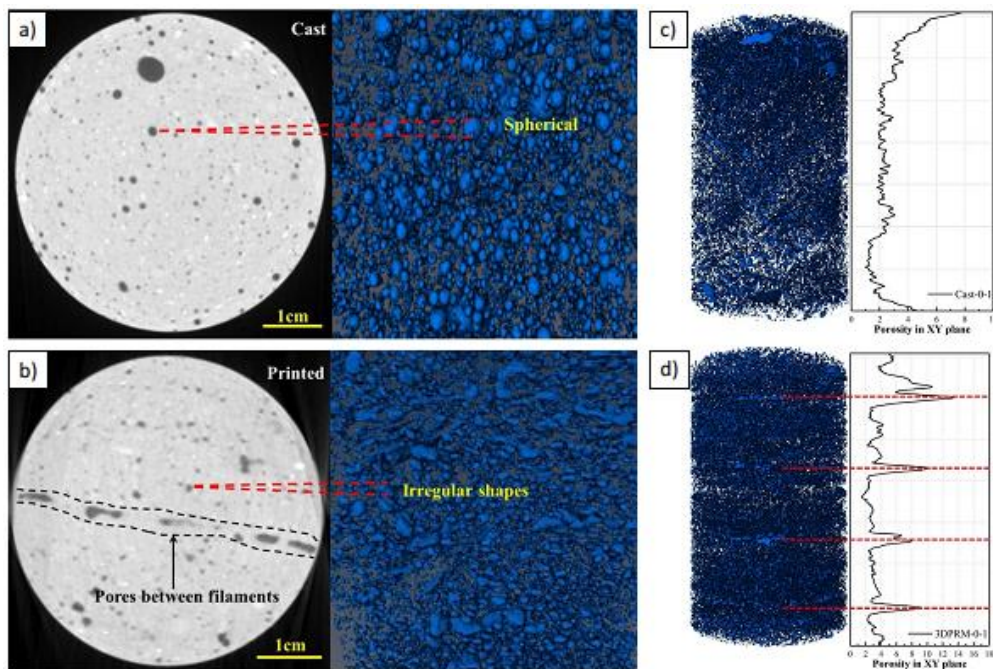
Source: Adapted from Mechtcherine *et al.* (2022) and Xu *et al.* (2021)

In their study, Liu *et al.* (2022a) investigated the mechanical behavior of 3DCP under compressive strength, splitting tensile strength, and flexural strength. The tests were conducted at different curing times (1, 4, 7, 14, and 28 days of curing) and load directions (X, Y, and Z directions). Furthermore, the pore structure and damage mechanism were characterized via X-ray computed tomography and DIC. The results were compared with mold-cast specimens for reference. The 3DCP material composition comprised Ordinary Portland cement, fly ash, silica fume, natural sand, high-efficient polycarboxylate-based superplasticizer, early strength agent, cellulose ethers, and polyvinyl alcohol fibers. The water-to-cement ratio was kept constant at 0.30. Moreover, the fluidity range required to achieve printability of the 3DCP was defined as 180 to 210 mm. The 3DCP specimens were saw-cut out of a 3D-printed element, produced using a gantry 3D printer with a 30 mm diameter printer head. The nozzle moved at a speed of 120 mm/s, and the extrusion speed was set at 200r/min. Each layer of the printed structure had dimensions of 15 mm in height and 31.50 mm in width. The compressive strength and splitting tensile strength tests were evaluated using cubic specimens of 100 mm side, while the three-point flexural strength specimens employed prisms with dimensions 40 x 40 x 160 mm.

The results of the compressive strength test at 28 days showed an average strength

reduction from mold-cast to 3D-printed specimens of 36%. The highest strength observed was 47.03 MPa in the mold-cast specimens. The DIC revealed that the damage pattern in cubes loaded in X and Y directions started at the edges of the specimens and extended gradually, while the cubes loaded in Z direction presented cracks that developed roughly at a diagonal 45-degree angle. Furthermore, successful stress predictions were achieved when cracks propagated perpendicular or parallel to the interlayer regions. The results of the splitting tensile strength test at 28 days indicated that the highest strength was exhibited by 3D-printed specimens loaded in the X-direction (4.93 MPa), followed by 3D-printed specimens in the Y and Z directions, and mold-cast specimens. In the three-point flexural strength test, 3D-printed specimens loaded in the Z-direction demonstrated the highest strength (6.91 MPa), followed by mold-cast specimens and 3D-printed specimens in the Y and X directions. Finally, the authors concluded that the pore structure of 3DCP differs significantly from that of mold-cast specimens. Notably, elongated pores found in 3D-printed specimens directly impacted their mechanical behavior, resulting in pronounced anisotropy. Figure 4.2 illustrate the pore morphology found in mold-cast and 3D-printed specimens, which can be associated with the research of Wu *et al.* (2023), where the porosity of 3D-printed specimens was higher in interlayer regions.

Figure 4.2 – Pore morphology and location. a) spherical pores of mold-cast specimens; b) irregular shaped pores of 3D-printed specimens; with higher porosity in the interlayer; c) pore distribution in mold-cast specimens; d) pore distribution in 3D-printed specimens, with higher porosity in the interlayers



Source: Adapted from Liu *et al.* (2022a) and Wu *et al.* (2023)

Yu *et al.* (2021) studied the microstructural characterization of 3DCP using Mercury Intrusion Porosimetry and X-ray computed tomography. Additionally, the mechanical performance of 3DCP along different directions (1, 2, and 3, equivalent to Z, Y, and X in this research, respectively) was examined. Both 3D-printed and mold-cast specimens were subjected to compressive strength and three-point flexural strength tests for comparison. The 3D-printing material consisted of ordinary Portland cement, fly ash, densified silica fume, three types of sieve-graded silica sands, polycarboxylate ether-based superplasticizer, commercially available retarder for OPC concrete, and tap water. The water-to-binder ratio was maintained constant at 0.31. The 3D printing system employed a gantry-style 3D printer with a circular nozzle measuring 30 mm in diameter, a progressive cavity pump, and a 3-meter-long hose. The printer operated at a speed of 30 mm/s, extruding material at a rate of 1.0 L/min and producing layers of 10 mm thickness. Cubic specimens of 35 mm side and prisms measuring 200 x 35 x 35 mm were saw-cut out of the 3D-printed hollow column.

The findings revealed an average strength reduction from mold-cast to 3D-printed specimens of 13% under compressive strength and 21% under flexural strength. In the three-point flexural strength test, the 3D-printed specimens tested in direction “3” (equivalent to X-direction in this research) exhibited the lowest strength. The authors emphasized that the impact of loading directions is more pronounced in flexural strength compared to compressive strength. Moreover, both MIP and C-ray CT analysis revealed that the 3D-printed specimens exhibited higher porosity compared to the mold-cast specimens. While the pores in the mold-cast specimens displayed a more spherical nature, the pores in the 3D-printed specimens were characterized by irregular and angular shapes. The authors concluded that the quantity and morphology of pores in 3D concrete printing (3DCP) are influenced by factors such as mix design, fabrication process, printer head movement, inadequate consolidation, and rapid water loss. Additionally, the reduced strength observed in the 3D-printed specimens can be attributed not only to the pore structure but also to the accelerated transport of moisture and fluid in the 3DCP technique.

In the study conducted by Ding *et al.* (2020) the impact of various factors on the mechanical performance of 3DCP was examined. These factors included the replacement ratio of recycled sand (12.5%, 25%, and 50% by weight of total fine aggregate), curing age (7, 14, and 28 days), nozzle height (0 mm, 5 mm, and 10 mm), and the direction of loading relative to the layer orientation (X, Y, and Z directions). The mechanical tests comprised compressive strength, splitting tensile strength, and four-point flexural strength tests. The results were

compared to mold-cast specimens for reference. Figure 4.3 illustrate the mechanical test setups. Furthermore, DIC analysis was carried out to capture the strain behavior and failure pattern of 3DCP. Additionally, SEM and EDS analyses were also performed. The material consisted of Ordinary Portland cement, river or recycled sand, high-efficiency polycarboxylate-based superplasticizer, hydroxypropyl methylcellulose, nano clay, and sodium gluconate. The sand-to-cement ratio and the water-to-cement ratio were kept constant at 1.0 and 0.305, respectively. From flow table tests, an initial fluidity was found to vary from 190 to 210 mm. The 3D printing system included a nozzle of 30 mm diameter nozzle, which extruded layers measuring 30 mm in width and 15 mm in height at a speed of 50 mm/s and a volumetric flow of 1.35 L/min. Concrete slabs were 3D-printed and cured for 28 days at a temperature of $20 \pm 2^\circ\text{C}$ and a relative humidity of $95 \pm 5\%$. After this period, cubic specimens of 70.7 mm side and prisms with dimensions 90 x 90 x 360 mm were saw-cut from the 3D-printed element.

Based on the results obtained through DIC analysis, the compressive strength tests revealed the rapid propagation of diagonal cracks in both the X and Z directions. In the Y-direction, the cracks primarily extended along the print layer interface, which experienced the most pronounced deformation. In the splitting tensile tests, the fracture surfaces displayed a parallel orientation to the loading direction, exhibiting little deviation from the mold-cast specimens. In the four-point flexural test, the cracks exhibited considerably slower propagation in the Y and Z directions compared to the X-direction. Notably, all mechanical tests underscored the clear anisotropy of the 3D-printed concrete. Furthermore, the results revealed that the 3D-printed specimens exhibited lower mechanical strengths than the mold-cast specimens, except for the flexural strength test loaded in the Z-direction. The authors concluded that the reduction in the strength of 3DCP under compression could be attributed to the presence of voids between the layers and the relatively weak bond strength between the interlayers.

Figure 4.3 – Mechanical tests setup. a) compressive strength; b) splitting tensile strength; c) four-point flexural strength



Source: Adapted from Ding *et al.* (2020)

The work of Wolfs, Bos, and Salet (2019) studied the relationship between interlayer interval time (15 s, 1 h, 4 h, 7 h, and 24 h), nozzle height (8.0 mm, 9.5 mm, and 11 mm), and surface dehydration (covered and uncovered) on the mechanical properties of 3DCP. The results were compared with mold-cast specimens for reference. The mechanical tests included compressive strength and splitting tensile strength performed on cubes of 40 mm side and three-point flexural strength conducted on prisms measuring 40 x 40 x 160 mm. The mechanical tests were performed in I, II, and III directions (equivalent to Z, Y, and X, respectively) for the effect of loading direction relative to layer orientation. The material used was a designed printable mortar containing Portland cement, siliceous aggregate, limestone filler, additives, rheology modifiers, and polypropylene fibers. The water-to-binder ratio was 0.495. The 3D printer setup consisted of a four-degree-of-freedom gantry system, an M-Tec Duo-mix 2000 mixer pump, and a 25.4 mm diameter and 10 m long hose. The printed layers were 50 mm in width and 9.5 mm in height. After printing, the wall was stored under a plastic sheet for 24 hours, then removed from the print bed and saw-cut to obtain the specimens. Following cutting, the surface of the specimens was smoothed, and they were stored in water until their testing age.

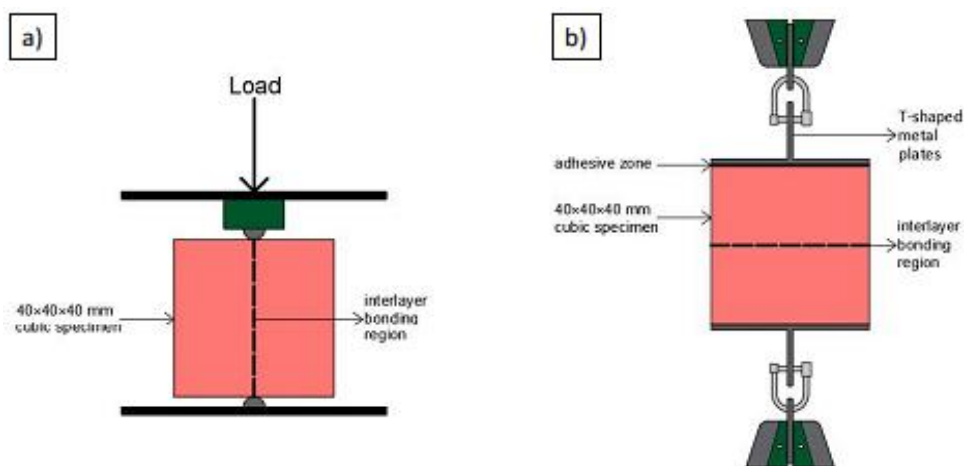
The results obtained from the three-point flexural strength test indicated a slightly lower strength of 3D-printed specimens loaded in the III direction (equivalent to the X direction in this study) than in the other two directions. Mold-cast specimens exhibited an approximately 31% higher compressive strength compared to 3D-printed specimens. Notably, no significant directional dependency was observed in the 3D-printed specimens under compression. Furthermore, as the time intervals increased, the mechanical strength of 3DCP decreased, impacting the failure mode of these specimens. In terms of dehydration, the uncovered specimens displayed smoother crack surfaces and higher void contents compared to the covered specimens. The authors concluded that among all the parameters investigated, longer time intervals for dehydration had the most significant quantitative effect on flexural strength. Additionally, it was highlighted that this influence may be stronger in practice, where there are no ideal curing conditions, emphasizing the need for quality control methods.

The work of Demiral *et al.* (2022) studied the anisotropy of 3DCP in terms of mechanical performance and bonding properties. The compressive strength, three-point flexural strength, splitting tensile strength, and direct tensile strength tests were performed on specimens at different curing ages (7, 28, and 90 days) and loading directions (perpendicular, parallel, and lateral to the printing direction, equivalent to Z, X, and Y directions in this research). The results were compared with mold-cast specimens for reference. Figure 4.4

illustrates a representation of the tensile strength tests. The material design included construction and demolition waste, fine recycled concrete aggregates, and two different types of alkaline activators. The water-to-binder ratio was maintained constant at 0.33. The 3D printing system comprised a gantry system 3D printer, a mortar pump, and a rectangular nozzle with a speed of 60 mm/s. The layers measured 20 mm in height and 40 mm in width. Immediately after printing, cubic specimens of 40 mm side and prismatic specimens measuring 40 x 40 x 160 mm were cut from the fresh printing using a thin finishing line. The curing process was performed under ambient conditions to simulate field applications.

The compressive strength test results indicated a strength improvement in 3D-printed specimens loaded in the Z-direction compared to mold-cast specimens, highlighting the presence of clear anisotropy in the 3D-printed specimens. Additionally, the three-point flexural strength test demonstrated that 3D-printed specimens loaded in the Z-direction exhibited the highest strength, followed by mold-cast specimens and 3D-printed specimens loaded in the Y-direction, respectively. Furthermore, the splitting tensile strength test, which assessed the interlayer strength of 3D-printed specimens, yielded results similar to those obtained from the direct tensile strength test. Based on these findings, the authors concluded that the 3D-printed specimens exhibited anisotropic behavior and that the 3D-printed specimens loaded in the Z-direction demonstrated superior performance compared to those loaded in the other two directions.

Figure 4.4 – Tensile strength tests. a) splitting tensile; b) direct tensile



Source: Adapted from Demiral *et al.* (2022)

Rahul *et al.* (2019) investigated the mechanical behavior of 3D-printed specimens subjected to compressive strength, three-point flexural strength, and direct bond shear tests in different loading directions (D3, D2, and D1, and E1, E2, and E3 equivalent to X, Y, and Z in this research, respectively). Additionally, the porosity was evaluated using the vacuum saturation method. The results were compared to those of mold-cast specimens for reference. The material consisted of Portland cement, fly ash, silica fume, attapulgite clay, polycarboxylic ether superplasticizer, hydroxypropyl methylcellulose base viscosity modifying agent, quartz sand and powder, and polypropylene fibers of 12 mm length and 40 μm thickness. The 3D printing system comprised a laboratory scale 3D printer, a nozzle of dimensions 30 x 30 mm, and an extrusion speed of 44 mm/s. Cubic specimens of 50 mm side and prismatic specimens measuring 160 x 40 x 40 mm were saw cut out of the 3D-printed element.

The findings indicated that the interlayer regions of the 3D-printed specimens exhibited higher porosity compared to the bulk regions within the layers. The compressive strength test revealed that the 3D-printed specimens had lower strengths compared to the mold-cast specimens. However, no significant anisotropic behavior was observed on the 3D-printed specimens under compression. In the three-point flexural strength test, a decrease in strength was only observed in the 3D-printed specimens tested in the E1-direction (equivalent to the X-direction in this study) when compared to the mold-cast specimens. Finally, the authors noted an evident anisotropic behavior in 3D-printed specimens subjected to flexural strength.

The research of Le *et al.* (2012) investigated the hardened properties of high-performance 3D-printed concrete. The density, compressive strength, four-point flexural strength, tensile bond strength, and drying shrinkage were tested and compared to mold-cast specimens for reference. In the mechanical tests, different loading directions were evaluated (I, II, and III, equivalent to Z, Y, and X in this research). The mix design included cement, fly ash, silica fume, sand, polycarboxylate-based superplasticizer, a retarded, and polypropylene microfibers. The water-to-binder ratio was maintained constant at 0.26, and the water-to-cement ratio was 0.37. Cubic specimens of 100 mm side and prismatic specimens measuring 100 x 100 x 400 mm were saw-cut out of the 3D-printed components.

The findings indicated a notable difference in density between the 3D printable concrete (ranging from 2250 to 2350 kg/m^3) and ordinary mortars as well as sprayed mortars (ranging from 1800 to 2000 kg/m^3). This disparity was attributed to the better grading and homogeneity found in the 3D-printed material. Furthermore, the compressive strength of 3D-printed specimens was found to be lower than that of mold-cast specimens, with minimal observed

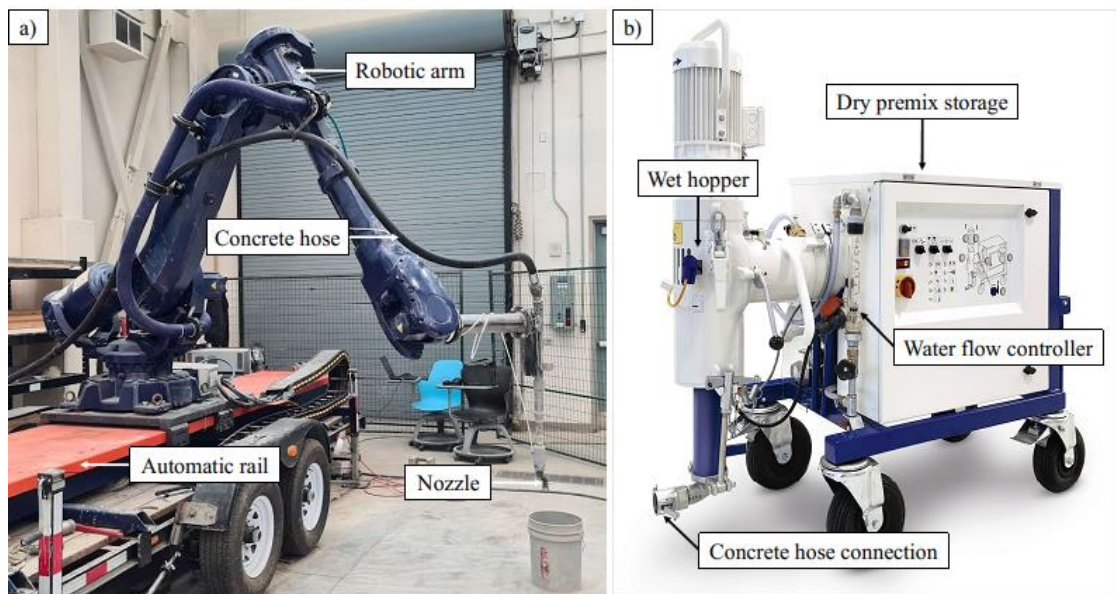
anisotropy. In the four-point flexural strength test, 3D-printed specimens loaded in the I and II directions (Z and Y directions in this study) displayed higher strength than the mold-cast specimens, while specimens loaded in the III direction (X direction in this study) exhibited the lowest flexural strength. Additionally, well-printed specimens demonstrated reduced porosity (1.0%) compared to mold-cast specimens (3.8%). Finally, the authors concluded that the anisotropy of the 3D-printed specimens inevitably impacted their hardened properties.

5. EXPERIMENTAL PROGRAM

5.1. 3D specimen preparation

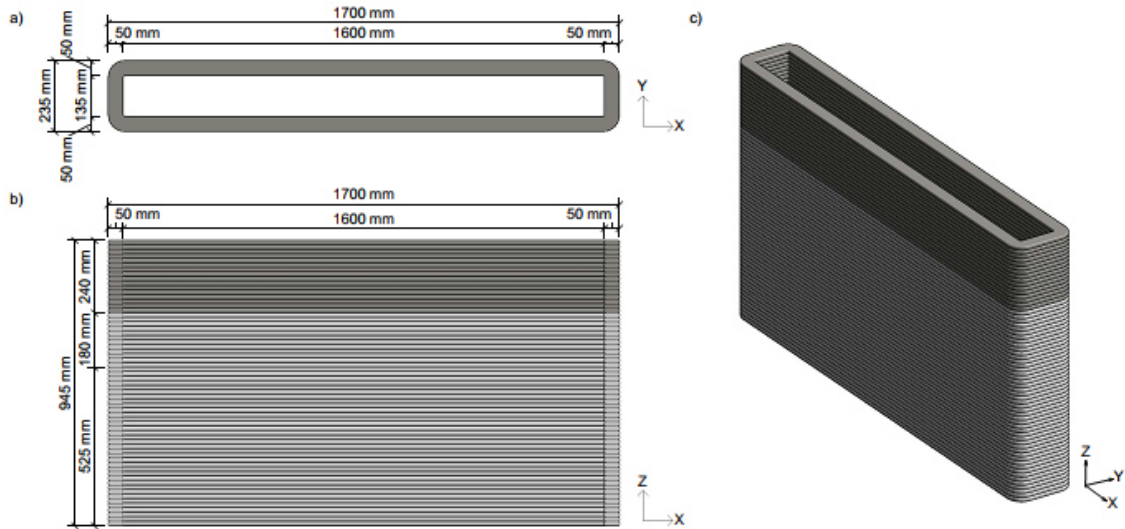
This research examined two groups of specimens: (i) specimens saw-cut of a 3D-printed wall and (ii) standard mold-cast specimens. The 3D printing system employed in this research consisted of a robotic arm connected to a mortar pump via a 13-meter-long hose with an internal diameter of 38.1 mm. The utilized material consisted of a proprietary and confidential dry premixed mortar purchased from a commercial supplier. The dry premixed mortar was mixed with water in the mortar pump before extrusion. The material was extruded via a 40 mm nozzle. The 3D-printed wall consisted of two 50 mm thick veneers enclosing a cavity with a width of 135 mm. The wall was 945 mm in height, 1700 mm in length, and 235 mm in total width. A visual representation of the 3D printing system and the wall can be found in Figures 5.1 and 5.2, respectively.

Figure 5.1 – Printing set up. a) robotic arm; b) similar pump used for printing



Source: Author (2023)

Figure 5.2 – 3D-printed wall design. a) floor plan; b) section; c) 3D view



Source: Author (2023)

The 3D printing process was executed over two days, with the printing parameters provided in Table 5.1. Simultaneously, three additional walls were printed, which served distinct research purposes. Figure 5.3 illustrate the 3D-printed walls over the two-days printing. The average layer time was 3 minutes and 04 seconds. The curing process involved spraying the walls with water and covering them with a plastic tarp for three consecutive days. Finally, on the 28th day, cubic and prismatic specimens were meticulously saw-cut from the designated 3D-printed wall.

Table 5.1 – Printing parameters

Printing parameters	First day	Second day
Number of layers printed	47	18
Total printing time	2 h 42 m	1 h 06 m
Layer time	2 m 47 s	3 m 20 s
Avg. Robot speed	107 mm/s	97 mm/s
Avg. Pump speed	30 Hz	33 Hz
Avg. Water flow	734 L/h	713 L/h
Avg. Print temperature	20.9 °C	20.2 °C

Source: Author (2023)

Figure 5.3 – 3D-printed walls. a) first day of printing; b) second day of printing



Source: Author (2023)

5.2. Mold-cast specimen preparation

The consistency between 3D-printed and mold-cast specimens was ensured using the same fluidity in both preparations. Following the ASTM International Standard C1437-20 (ASTM INTERNATIONAL, 2020a), hydraulic cement mortar flow tests were carried out under two different conditions. Initially, two tests were conducted during the 3D printing process, utilizing the material in its extruded state from the nozzle. Subsequently, four additional tests were performed manually, with varying water content, until the test results matched those obtained during the 3D printing of the walls. The water-to-dry premixed mortar ratio, indicative of the fluidity matching that of the 3D-printed walls, was determined to be 0.193. This ratio corresponded to an average fluidity of 175 mm, slightly lower than observed in prior studies, which exhibited fluidity ranges varying from 180 to 210 mm (DING et al., 2020; LIU et al., 2022a). The test results are presented in Table 5.2.

The procedure started with the cleaning and drying of the flow table, followed by the placement of the flow mold at its center. A layer of mortar, measuring approximately 25 mm in thickness, was placed inside the mold and tampered 20 times. Subsequently, the remaining volume of the mold was filled with mortar and subjected to an additional 20 tampering motions. Any surplus mortar on the top surface of the mold was removed to attain a level plane, and the upper surface of the flow table was once again cleaned. The mold was lifted away from the table, and the table was dropped 25 times within a 15-second interval. The diameter of the

spread mortar was measured four times. The average of these readings was subtracted from the initial diameter, yielding a percentage increase in diameter.

Table 5.2 – Hydraulic cement mortar flow tests results

Test	D1	D2	D3	D4	Avg. D	Spread	Initial D.	Increase (%)
3D 1	175	174	177	177	176	3	100	76
3D 2	173	172	174	172	173	2	100	73
0.158	129	130	126	128	128	4	100	28
0.190	171	172	172	176	173	5	100	73
0.195	176	176	176	176	176	0	100	76
0.200	182	182	180	185	182	5	100	82

Measurements in millimeters.

Source: Author (2023)

The mold-cast specimens were prepared using the determined water-to-dry premixed mortar ratio. The dry premixed mortar was placed in a mechanical batter, and after all the water was added, the material was mixed for 3 minutes. The 50 mm side cubes were prepared according to the ASTM International Standard C109/C109M-21 (ASTM INTERNATIONAL, 2021a). First, a layer of material of about 25 mm thickness was placed and tampered 32 times in about 10 seconds in four rounds, then the rest of the mold was filled with mortar and tampered again as specified for the first layer. The extra mortar on the top of the molds was leveled with a trowel, and the specimens were vibrated until their upper surface appeared to be more evenly distributed and homogeneous.

The 150 x 50 x 50 mm prisms were prepared according to the ASTM International Standard C348-21 (ASTM INTERNATIONAL, 2021b). First, a layer of material of about 20 mm thickness was placed in the mold and tampered with 12 strokes, applied in three rounds of four strokes each, and completed in about 15 seconds. The rest of the mold was then filled with mortar and tampered again in the same manner as in the bottom layer. The excess material on the top of the molds was leveled with a trowel, and the specimens were vibrated until their upper surface appeared to be more evenly distributed and homogeneous. After a period of 24 hours, the specimens were unmolded, sprayed with water, and covered with a plastic tarp for a continuous duration of three days. This curing method was the same as the approach used on the 3D-printed walls. The mold-cast specimens can be seen in Figure 5.4.

Figure 5.4 – Mold-cast specimens



Source: Author (2023)

5.3. Test Matrix

The test matrix comprised various tests focused on material, physical, mechanical, and microstructural properties, as outlined in Table 5.3. The interlayer bond strength was evaluated through three distinct tests: (iii.c) splitting tensile strength, (iii.d) three-point flexural strength, and (iii.e) four-point flexural strength. The pulse velocity and the mechanical tests were performed in three directions: X, Y, and Z. The X-direction corresponds to the printing direction, the Y-direction is perpendicular to the X-direction, and the Z-direction is perpendicular to the XY plane and refers to the height of the printing. The microstructural tests were performed on XY and YZ planes. The mechanical tests and their respective directions are illustrated in Figure 5.5.

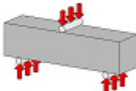
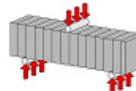
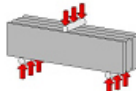
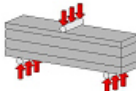
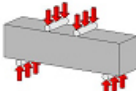
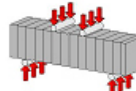
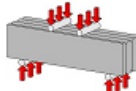
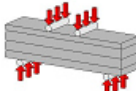
Table 5.3 – Performed tests

Properties	Tests	Specimen*
i. Material	a. Flow of hydraulic cement mortar	Mortar
	b. Sieve analysis of fine and coarse aggregates	Dry premix
	c. Particle size distribution (PSD)	Dry premix
	d. X-ray fluorescence (XRF)	Dry premix
ii. Physical	a. Density, absorption, and voids	Cube
	b. Ultrasonic pulse velocity (UPV)	Cube
iii. Mechanical	a. Compressive strength	Cube
	b. Oblique shear strength	Cube
	c. Splitting tensile strength	Cube
	d. Three-point flexural strength	Prism
	e. Four-point flexural strength	Prism
iv. Microstructural	a. Scanning electron microscopy (SEM) and energy-dispersive x-ray spectroscopy (EDS)	Fragment

* Cube: 50 mm; Prism: 50 x 50 x 200 mm; Fragment: approximately 50 x 20 x 15 mm

Source: Author (2023)

Figure 5.5 – Mechanical tests and load direction

GROUP	MOLD-CAST	3D-PRINTED			
		-	X	Y	Z
LOAD DIRECTION	-	X	Y	Z	
COMPRESSION					
OBLIQUE SHEAR					
SPLITTING TENSILE					
THREE-POINT FLEXURAL					
FOUR-POINT FLEXURAL					

Source: Author (2023)

Furthermore, specimens tested in the Y-direction were capped with rapid-setting cement-based concrete repair mortar to ensure a uniform load application during the mechanical tests, as shown in Figure 5.6. The concrete repair mortar, mixed with water at a 0.200 water-to-binder ratio, exhibited a compressive strength of 39.3 MPa at 28 days, according to its technical specifications. The mechanical tests were administered with an MTS machine and an additional load cell of 200 kN capacity. The DIC technique was employed to examine the strain behavior and crack propagation on the surface of the specimens. The DIC process involved applying a stochastic pattern (speckle) to the front surface of the specimens and capturing images every 2 seconds during the test with a camera connected to a Data Acquisition System. These images were then processed using the GOM Correlate Pro software (GOM, 2022). The speckle painting and the mechanical test setup can be seen in Figure 5.6.

Figure 5.6 – Testing process. a) capping of 3D-printed specimens for loading in the Y-direction; b) speckle pattern made on the front surface of the specimens; c) mechanical test setup



Source: Author (2023)

5.3.1. Sieve analysis of fine and coarse aggregates

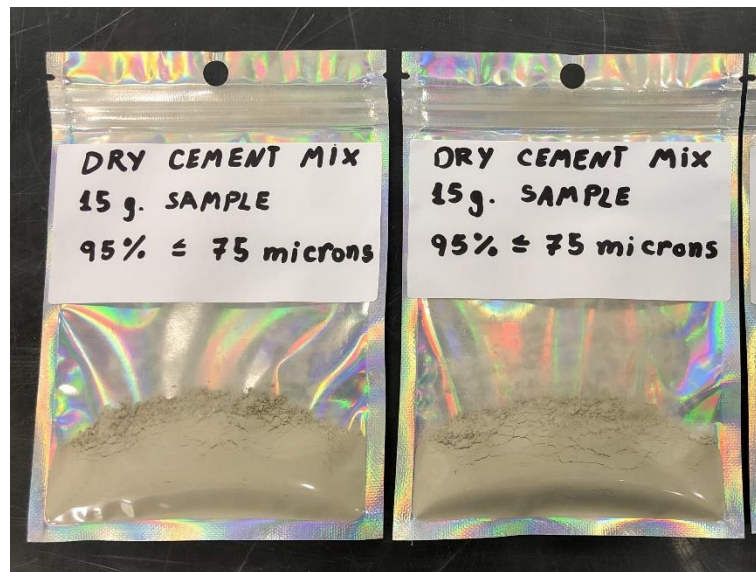
The sieve analysis of fine and coarse aggregates was performed in accordance with ASTM International Standard C136/C136M-19 (ASTM INTERNATIONAL, 2020b). First, 1 kg of dry premixed mortar was placed in an oven at 110°C for 24 hours. Then, the seven test sieves were mounted in decreasing sizes of the opening from top to bottom, according to

ASTM International Standard E11-20 (ASTM INTERNATIONAL, 2020c). Next, the dry material was weighed again, placed inside the top sieve, and agitated in the mechanical sieving machine for 10 minutes. Finally, the mass of material retained in each of the seven sieves was weighted, and the fineness modulus was calculated.

5.3.2. Particle size distribution (PSD) and x-ray fluorescence (XRF)

The laser diffraction particle size distribution (PSD) and the X-ray fluorescence (XRF) analyses were carried out by a contracted laboratory. The preparation of the test samples for the PSD and XRF tests involved collecting 15 g of material retained in test sieve No. 200, which corresponded to $95\% \leq 75$ microns. The test samples can be seen in Figure 5.7.

Figure 5.7 – Samples for PSD and XRF analyses



Source: Author (2023)

5.3.3. Density, absorption, and voids

The density, absorption, and voids test was carried out according to the ASTM International Standard C642-21 (ASTM INTERNATIONAL, 2021c). Firstly, the cubic specimens of 50 mm side were weighed and dried in an oven at 110°C for 24 hours. After being removed from the oven, they cooled in dry air to a temperature of 20°C to 25°C and weighed again. This process was repeated until the difference between any two successive values was less than 0.5 % of the lowest value obtained. The last obtained value, the oven-dry mass, was

designated “A”. Secondly, the specimens were immersed in water at 21°C for 48 hours until two successive values of the mass of the surface-dried sample at intervals of 24 h showed an increase in mass of less than 0.5 % of the larger value. After that, the specimens were surface-dried with a towel and weighed. Next, the specimens were placed inside a pan, covered with tap water, and boiled for 5 h. The pan was allowed to cool by natural loss of heat for at least 14 h, to a final temperature of 20°C to 25°C. Then, the surface moisture of the specimens was removed with a towel, and their mass was determined. The soaked, boiled, surface-dried mass was designated “C”. Finally, the specimens were suspended by a wire, and their apparent mass in water “D” was determined. The volume of permeable voids was calculated according to Equation 5.1.

$$\text{Volume of permeable voids (\%)} = \left[\frac{(C - A)}{(C - D)} \right] * 100 \quad \text{Equation 5.1}$$

Where:

A: mass of oven-dried sample in air (g).

C: mass of surface-dry sample in air after immersion and boiling (g).

D: apparent mass of sample in water after immersion and boiling (g).

5.3.4. Ultrasonic pulse velocity (UPV)

The ultrasonic pulse velocity test (UPV) was performed on cubic specimens of 50 mm side according to the ASTM International Standard C597-16 (ASTM INTERNATIONAL, 2016a). The equipment used was the Ultrasonic Pulse Velocity Tester CN842. First, a coupling agent (such as petroleum jelly or grease) was applied to the faces of the Transmitting Transducer and the surfaces of the specimen. Next, the transducers were pressed firmly on directly opposite sides of the specimen. The transit time was given by the Pulse Generator, and the pulse velocity was calculated according to Equation 5.2. This test is used to assess the uniformity and quality of the material, as it indicates the presence of voids and cracks in the specimen.

$$V = \frac{L_t}{T_t} \quad \text{Equation 5.2}$$

Where:

V: pulse velocity (m/s).

L_t : distance between centers of transducer faces (m).

T_t : transit time (s).

5.3.5. Compressive strength

The compressive strength test was conducted on cubic specimens of 50 mm side in conformity with the ASTM International Standard C109/C109M-21 (ASTM INTERNATIONAL, 2021a). First, any loose material or incrustation was removed from the surface of the specimen. Then, the specimen was placed on the testing machine and subjected to a loading rate ranging from 900 to 1800 N/s. The maximum applied load was recorded, and the compressive strength was calculated using Equation 5.3.

$$f_m = \frac{P}{A_s} \quad \text{Equation 5.3}$$

Where:

f_m : compressive strength (MPa).

P: maximum applied load (N).

A_s : area of loaded surface (mm²).

5.3.6. Oblique shear strength

The oblique shear strength test was performed on cubic specimens of 50 mm side in accordance with the methodologies proposed by Xu *et al.* (2021) and Yao *et al.* (2022). Two steel molds were fabricated to ensure a consistent 60-degree angle of the specimen. The specimen was subjected to a loading rate ranging from 1122.5 to 1326.5 N/s until its failure. The maximum applied load was recorded, and the shear strength was calculated according to Equation 5.4.

$$\tau = \frac{P \sin \alpha}{A_f} \quad \text{Equation 5.4}$$

Where:

τ : shear strength (MPa).

P: maximum applied load (kN).

α : inclination angle of the specimen ($^{\circ}$).

A_f: fracture area of the specimens (mm²).

5.3.7. *Splitting tensile strength*

The splitting tensile strength test was adapted from the ASTM International Standard C496/C496M-17 (ASTM INTERNATIONAL, 2017) because the thickness of the veneers precluded the extraction and testing of cylinders in X, Y, and Z directions (MECHTCHERINE et al., 2022). Consequently, in line with established protocols from prior studies (DEMIRAL et al., 2022; DING et al., 2020; KEITA et al., 2019; LIU et al., 2022a; ROUSSEL, 2018; WOLFS; BOS; SALET, 2019), cubic specimens of 50 mm side were employed in lieu of cylindrical specimens. Two steel bearing strips, measuring 65 x 8 x 3 mm, were placed at the top and bottom of the specimen along its central plane. The load was incrementally increased within a range of 45.8 to 91.6 N/s. The maximum applied load was recorded, and the splitting tensile strength was calculated using Equation 5.5.

$$T = \frac{2P}{\pi lc} \quad \text{Equation 5.5}$$

Where:

T: splitting tensile strength (MPa).

P: maximum applied load (N).

l: length of the line of contact with the specimen (mm).

c: cross-section of the specimen (mm).

5.3.8. *Three-point flexural strength*

The three-point flexural test was performed on prismatic specimens of 200 x 50 x 50 mm in accordance with the ASTM International Standard C293/C293M-16 (ASTM INTERNATIONAL, 2016b). The prisms were ground or capped to eliminate any gap more than 0.10 mm in width. The lower rigid supports were set at a span length of 150 mm, and the

upper loading block was aligned with the center of the specimen. The load was applied at a constant rate of 8.3 to 11.1 N/s, calculated according to Equation 5.6 until rupture occurred.

$$r = \frac{2Sbd^2}{3L} \quad \text{Equation 5.6}$$

Where:

r: loading rate (N/min).

S: rate of increase in the maximum stress on the tension face (MPa/min).

b: average width of the specimen (mm).

d: average depth of the specimen (mm).

L: span length (mm).

After the test was done, the average width and depth across one of the fractured faces were recorded. If the fracture occurred at a capped section, the cap thickness was included in the measurements. The modulus of rupture was then calculated according to Equation 5.7.

$$R = \frac{3PL}{2bd^2} \quad \text{Equation 5.7}$$

Where:

R: flexural strength (MPa).

P: maximum applied load (N).

L: span length (mm).

b: average width of the specimen (mm).

d: average depth of the specimen (mm).

5.3.9. *Four-point flexural strength*

The four-point flexural strength test was conducted on prismatic specimens of 200 x 50 x 50 mm in compliance with the ASTM International Standard C78/C78M-21 (ASTM INTERNATIONAL, 2021d). Leather shims were used to eliminate any gap between the specimen and the upper loading blocks that exceeded 0.10 mm in width. The lower rigid supports were set at a span length of 150 mm, while the upper loading blocks were 50 mm apart

and positioned 25 mm away from the center of the specimen. The load was applied at a constant rate of 12.5 to 16.7 N/s, calculated according to Equation 5.8 until rupture occurred.

$$r = \frac{Sbd^2}{L} \quad \text{Equation 5.8}$$

Where:

r: loading rate (N/min).

S: rate of increase in the maximum stress on the tension face (MPa/min).

b: average width of the specimen (mm).

d: average depth of the specimen (mm).

L: span length (mm).

After the test was done, the average width and depth across one of the fractured faces were recorded. If the fracture occurred at a capped section, the cap thickness was included in the measurements. In case the fracture was initiated in the tension surface within the middle third of the span length, the modulus of rupture was calculated according to Equation 5.9. Otherwise, Equation 5.10 was used.

$$R = \frac{PL}{bd^2} \quad \text{Equation 5.9}$$

$$R = \frac{3Pa}{bd^2} \quad \text{Equation 5.10}$$

Where:

R: flexural strength (MPa).

P: maximum applied load (N).

L: span length (mm).

b: average width of the specimen (mm).

d: average depth of the specimen (mm).

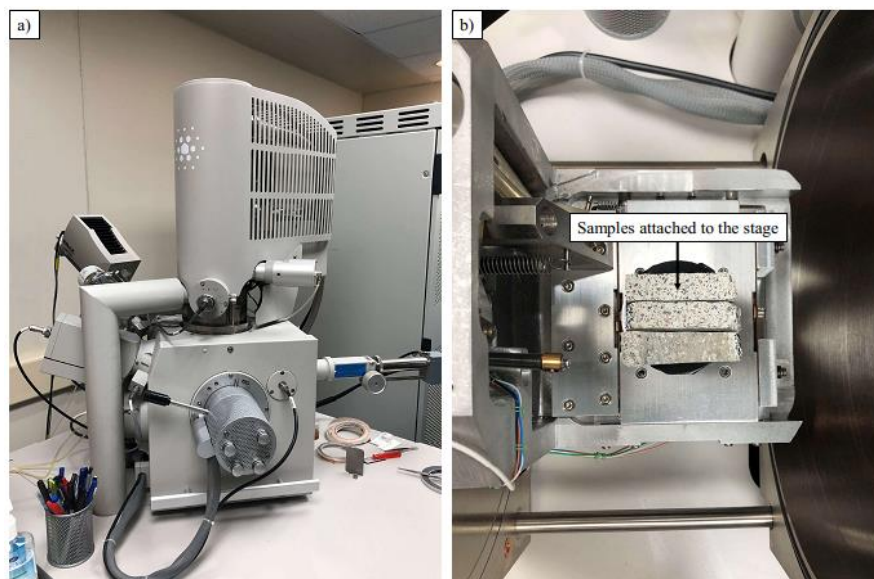
a: average distance between the line of fracture and the nearest support measured on the tension surface of the beam (mm).

5.3.10. Scanning electron microscope (SEM) and energy-dispersive x-ray spectroscopy (EDS)

According to the ASTM International Standard C1723-16 (ASTM INTERNATIONAL, 2016c), the SEM and EDS analyses involve the utilization of specialized equipment that generates an electron beam via a heating filament commonly composed of tungsten. This electron beam is repetitively scanned across the sample, releasing electrons that are then accelerated toward the sample through the application of an electric potential. The emitted electrons are subsequently focused onto a screen through a series of lenses and apertures, resulting in the formation of an image (SEM). Furthermore, the electron beam stimulates atoms within the sample, leading to the emission of X-rays with characteristic energies. These X-rays are measured by a solid-state detector, which records both their intensity and energy (EDS).

The analyses were conducted using the environmental FEI Quanta 200 FEG. Initially, the specimens were sectioned into samples measuring approximately 50 x 20 x 15 mm. Subsequently, compressed air was applied to the samples to remove any debris or dust particles. Finally, the samples were securely mounted onto the sample stage using double-sided tape. The images were captured with a high voltage of 15.0 kV, at magnifications ranging from 30x to 1500x, and analyzed using the Edax Octane Plus SDD, Team, and Scandium software. The equipment and test setup can be observed in Figure 5.8.

Figure 5.8 – SEM and EDS analyses. a) environmental FEI Quanta 200 FEG; b) samples attached to the stage



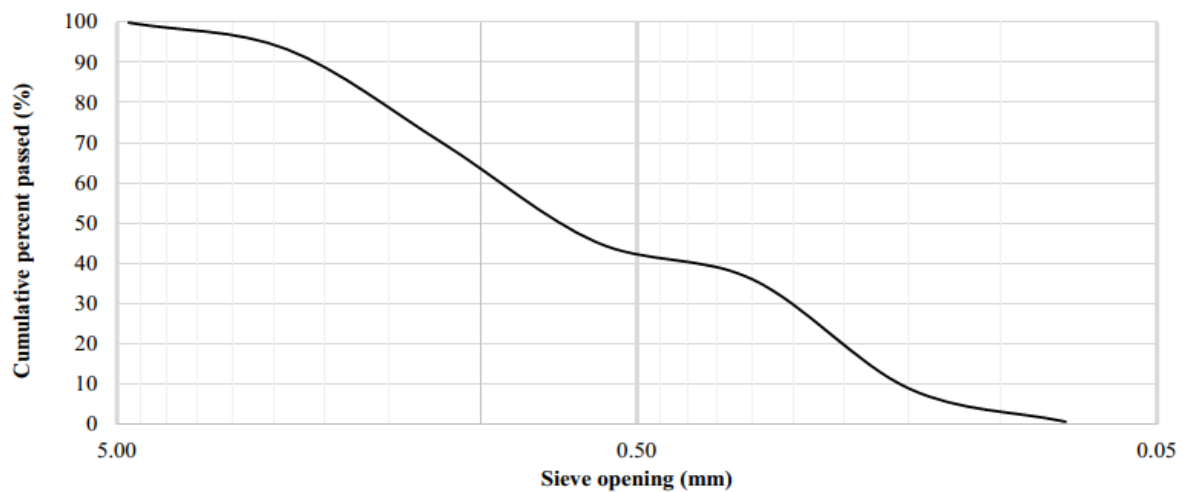
Source: Author (2023)

6. RESULTS AND DISCUSSION

6.1. Material tests

The sieve analysis of fine and coarse aggregates yielded a fineness modulus of 3.46. Figure 6.1 presents a graphical representation of the sieve analysis results. Notably, the presence of fibers was observed during the sieving process. Figure 6.2 provides a visual depiction of the fibers, which had an average length of 7.0 mm. The laser diffraction PSD test generated percentile values “D” which indicate the size below which 10%, 50%, and 90% of the particles fall. These values were $D(0.10) = 4.97 \mu\text{m}$, $D(0.50) = 14.43 \mu\text{m}$, and $D(0.90) = 31.35 \mu\text{m}$. The PSD test results are displayed in Figure 6.3. With the findings from the sieve analysis and the PSD test, the material was determined to possess a good degree of homogeneity and particle size distribution. Furthermore, the data obtained from the XRF analysis are described in Table 6.1.

Figure 6.1 – Cumulative percent passed vs. sieve opening curve



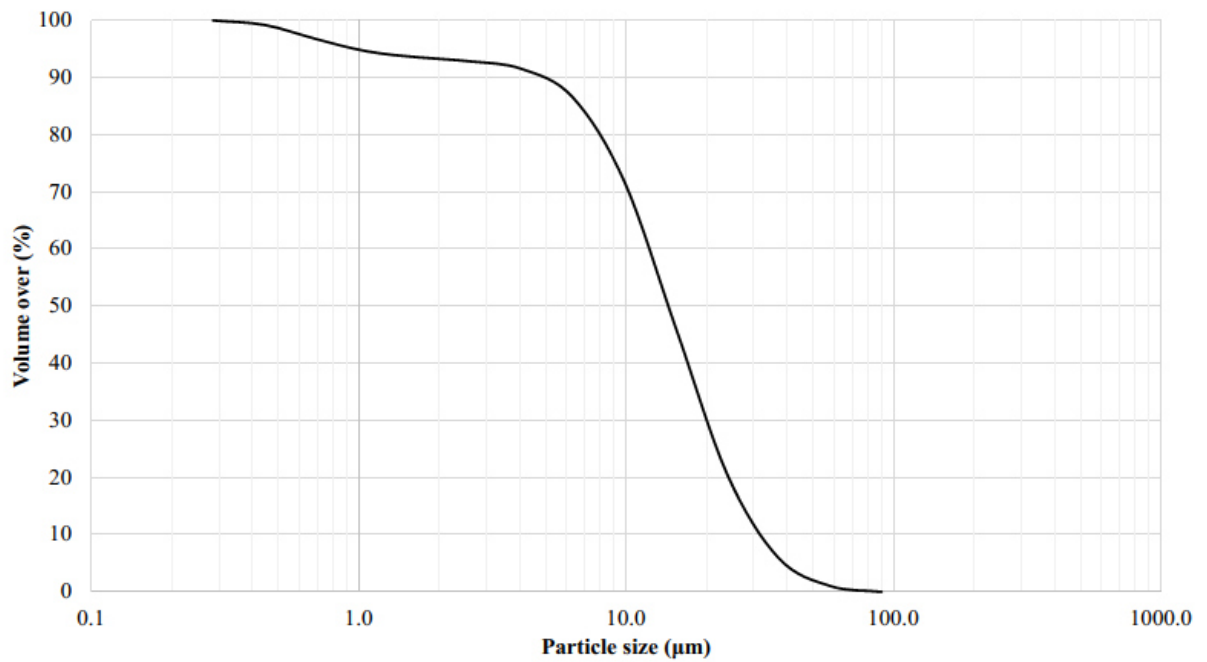
Source: Author (2023)

Figure 6.2 – Fibers found during the sieve analysis of fine and coarse aggregates, ruler for scale, in inches



Source: Author (2023)

Figure 6.3 – Volume over vs. particle size curve



Source: Author (2023)

Table 6.1 – Chemical composition of the dry premixed mortar

Analyte symbol	Analyte name	Dry premix (%)
CaO	Calcium oxide	60.8
SiO ₂	Silicon dioxide	18.2
Al ₂ O ₃	Aluminum oxide	4.5
MgO	Magnesium oxide	2.6
Fe ₂ O ₃ (T)	Iron(III) oxide	1.6
K ₂ O	Potassium oxide	0.7
Na ₂ O	Sodium oxide	0.3
P ₂ O ₅	Phosphorus pentoxide	0.2
TiO ₂	Titanium dioxide	0.2
MnO	Manganese(II) oxide	0.1
Cr ₂ O ₃	Chromium(III) oxide	< 0.01
Loss on ignition (LOI)		6.8
Total		95.8

Source: Author (2023)

6.2. Physical tests

The experimental data presented in Table 6.2 highlights the average density of the mold-cast and the 3D-printed specimens as 2195 Kg/m³ and 2205 Kg/m³, respectively. These values surpass the density observed in typical mortar specimens (LE et al., 2012), which can be attributed to the homogeneous particle size distribution observed in the material tests (Figures 6.1 and 6.3). Additionally, the results of the density, absorption, and voids test revealed that the 3D-printed specimens exhibited an average density 0.5% higher and a total void volume 6% lower than the mold-cast specimens. Analogous findings were documented in previous research conducted by (HEEVER et al., 2022; LE et al., 2012). According to Le *et al.* (2012), these outcomes affirm the successful printing of the 3D wall, suggesting that the layer time (Table 5.1) was sufficiently short to create a cohesive interlayer bond with lower porosity. Notably, previous research has shown that longer layer times can negatively affect the hydration of the interlayer surface, increase porosity, decrease density, and result in larger pore sizes in the interlayer (KRUGER; DU PLESSIS; VAN ZIJL, 2021; LIU et al., 2022b; MEURER; CLASSEN, 2021; WOLFS; BOS; SALET, 2019; XU et al., 2021).

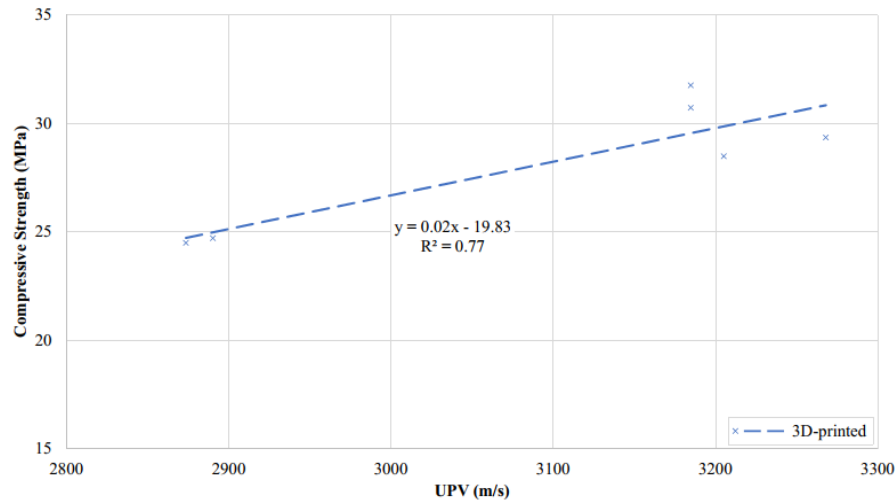
Table 6.2 – Results from the physical tests

Cubic specimens	Avg. Density (Kg/m³)	Avg. Total void volume (%)	Direction	Avg. Pulse velocity (m/s)
Mold-cast	2195 (0.8)	21.6 (1.4)	-	3572 (0.7)
			X	3237 (1.0)
			Y	2882 (0.3)
			Z	3185 (0.0)
			Avg.	3101
3D-printed	2205 (2.1)	20.4 (1.7)	p value	.002
			Anisotropy	
			COV in percentage inside parenthesis. ANOVA with significance level $p=0.05$.	

Source: Author (2023)

The UPV test results, shown in Table 6.2, revealed that the average pulse velocity of the 3D-printed specimens measured 3101 m/s, which was 13% lower compared to the mold-cast specimens. Particularly, the mold-cast specimens exhibited the highest pulse velocity, followed by the 3D-printed specimens in X, Y, and Z directions. The ANOVA confirmed a significant variance among these three directions, validating the anisotropic behavior of the 3D-printed specimens. Moreover, Figure 6.4 provides a visual representation of the relationship between compressive strength and UPV for 3D-printed specimens. The experimental results of 3D-printed cubes are represented by x-shaped markers. The correlation line for 3D-printed specimens was obtained through linear regression analysis and is shown as a dashed line, described by Equation 6.1. This equation is valid for analogous 3D-printed structures with compressive strengths varying from 25 to 32 MPa. The results obtained from the UPV test demonstrated its utility as a valuable tool for quality control and on-site compressive strength prediction of 3D-printed structures.

Figure 6.4 – UPV vs. compressive strength graphic



Source: Author (2023)

$$y = 0.02x - 19.83$$

Equation 6.1

6.3. Mechanical tests

The mechanical test results are presented in Table 6.3. In general, the 3D-printed specimens exhibited an average strength reduction of 43% across all tests when compared to the mold-cast specimens. Specifically, the results revealed an average strength reduction of 46% in the compressive strength test, 48% in the oblique shear strength test, 45% in the splitting tensile strength test, 36% in the three-point flexural strength test, and 43% in the four-point flexural strength test. This discrepancy in strength can be attributed primarily to the distribution of pores within the 3D-printed specimens, which tends to concentrate on the interlayers, generating a weaker interface than the rest of the layer areas (CHEN et al., 2022b; DEMIRAL et al., 2022; LIU et al., 2022a, 2022b; VAN DEN HEEVER et al., 2022b; WU et al., 2023; YU et al., 2021).

The coefficient of variance was calculated, conforming to each test standard. In the case of the oblique shear test, the values of $1s\%$ and $d2s\%$ were considered 5% and 14%, respectively, following the ASTM International Standard C670-15 (ASTM INTERNATIONAL, 2015). Furthermore, the ANOVA with a significance level of $p=0.05$ was employed to assess the difference in the behavior of X, Y, and Z directions of the 3D-printed specimens. The ANOVA results indicated anisotropy in the 3D-printed specimens for all tests except for the splitting tensile test.

Table 6.3 – Results of mechanical tests

Test	Avg. Strength (MPa)			Loss of strength (%)		
	Mold-cast	3D-printed				
Compressive strength	55.8	(0.6)	X	28.9	(1.5)	45
			Y	24.6	(0.4)	53
			Z	34.8	(1.5)	38
			Avg.	29.4	-	45
			p value	.001	Anisotropy	
Oblique shear strength	24.4	(0.1)	X	10.1	(6.4)	59
			Y	13.6	(5.4)	45
			Z	14.2	(4.5)	42
			Avg.	12.6	-	48
			p value	.04	Anisotropy	
Splitting tensile strength	5.1	(0.3)	X	2.6	(2.4)	50
			Y	3.0	(4.3)	41
			Z	2.8	(11.3)	45
			Avg.	2.8	-	45
			p value	.30	Isotropy	
Three-point flexural strength	5.7	(3.8)	X	2.6	(6.7)	54
			Y	4.7	(3.9)	18
			Z	3.7	(1.9)	35
			Avg.	3.7	-	36
			p value	.006	Anisotropy	
Four-point flexural strength	5.5	(0.9)	X	2.7	(4.3)	51
			Y	3.2	(1.6)	41
			Z	3.4	(3.4)	38
			Avg.	3.1	-	43
			p value	< .001	Anisotropy	

COV in percentage inside parenthesis. ANOVA with significance level $p=0.05$.

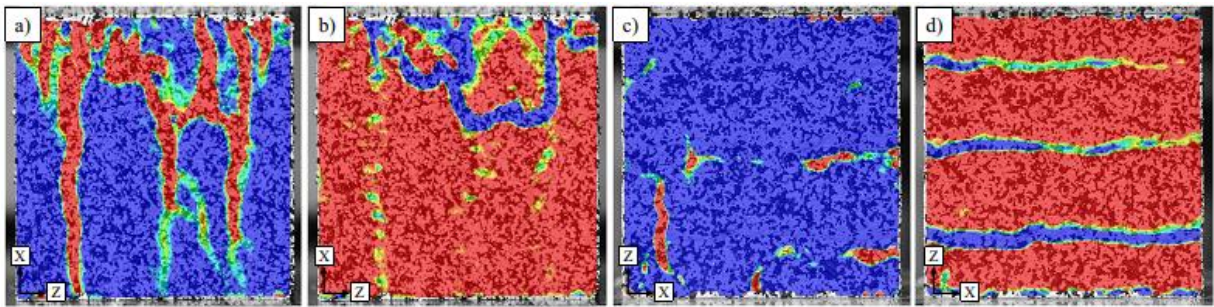
Source: Author (2023)

6.3.1. Compressive strength

The results of the compressive strength test yielded a 45% strength reduction between mold-cast and 3D-printed specimens, as described in Table 6.3. This reduction in strength aligns with findings from previous studies (CHO et al., 2019; DING et al., 2020; LE et al., 2012; LIU et al., 2022a; MEURER; CLASSEN, 2021; ÖZALP; YILMAZ, 2020; RAHUL et al., 2019; WOLFS; BOS; SALET, 2019; YU et al., 2021). Furthermore, the present research identified an anisotropic behavior in the 3D-printed specimens, as confirmed by the ANOVA in Table 6.3. This anisotropy of 3D-printed specimens under compressive strength has been consistently observed in earlier investigations (DEMIRAL et al., 2022; DING et al., 2020; LE et al., 2012; LIU et al., 2022a; MECHTCHERINE et al., 2019b; MEURER; CLASSEN, 2021).

Additionally, the compressive strength test showed low COV values for each specimen group, establishing its validity as an effective method for evaluating the compressive strength of 3D-printed components (refer to Table 6.3). The DIC analysis of the compressive strength tests, depicted in Figure 6.5, revealed cracks that aligned distinctly with the interlayers, with major and minor strains manifesting perpendicularly to one another. These results did not agree well the findings reported in two previous studies (DING et al., 2020; LIU et al., 2022a), as no diagonal cracks or significant deviations among the loading directions were detected in the present research.

Figure 6.5 - DIC analysis of the 3D-printed specimens under compressive strength. a) principal major strain of cubes tested in X-direction; b) principal minor strain of cubes tested in X-direction; c) principal major strain of cubes tested in Z-direction; d) principal minor strain of cubes tested in Z-direction



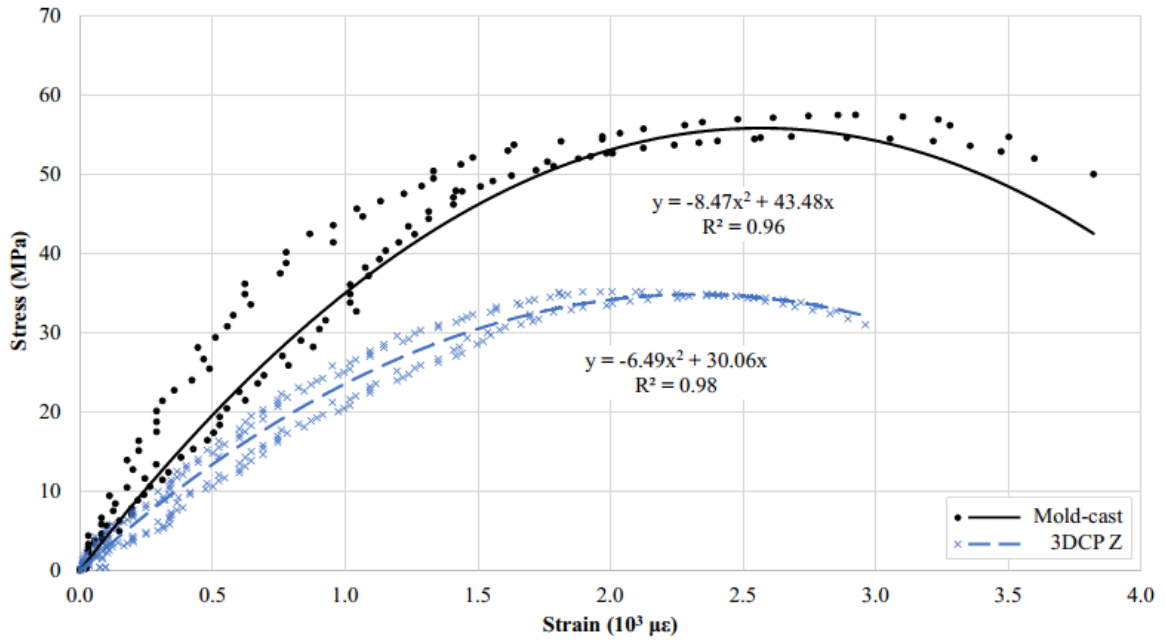
Source: Author (2023)

Figure 6.6 illustrates the stress *vs.* strain characteristics of mold-cast cubes and 3D-printed cubes tested in the Z-direction, providing a comprehensive analysis of their mechanical behavior. The experimental results of mold-cast cubes, obtained through DIC, are graphically represented by round dots. Similarly, the experimental results of 3D-printed cubes tested in the Z-direction, acquired using DIC, are depicted by x-shaped markers. The stress *vs.* strain curves were derived through 2nd degree polynomial regression analysis based on the experimental data of both specimens. The correlation curve for mold-cast cubes is visually represented by a continuous curve, denoting Equation 6.2. Correspondingly, the correlation curve for 3D-printed cubes tested in Z-direction is represented by a dashed curve, indicating Equation 6.3.

The findings derived from Equation 6.3, representing the behavior of 3D-printed cubes in the Z-direction, reveal reductions in stiffness (31%), stress capacity (38%), and strain (10%) when compared to the results obtained from Equation 6.2, which represents the behavior of mold-cast cubes. These comparative results are summarized in Table 6.4. These mathematical

formulations can serve as valuable tools for prospective investigations on the numerical modeling of analogous 3D-printed structures and future research. This stress-strain relationship of Equation 6.3 can be used by practicing engineers for designing 3D-printed structural elements.

Figure 6.6 – Stress vs. strain curves



Source: Author (2023)

$$y = -8.47x^2 + 43.48x \quad \text{Equation 6.2}$$

$$y = -6.49x^2 + 30.06x \quad \text{Equation 6.3}$$

Table 6.4 – Compressive strength results obtained from the stress vs. strain curves

Stress vs. strain curve results	Mold-cast	3DCP Z	Loss (%)
E (GPa)	36.4	25.1	31
σ_{cu} (MPa)	55.8	34.8	38
ϵ_0 ($\mu\epsilon$)	2567	2317	10

Source: Author (2023)

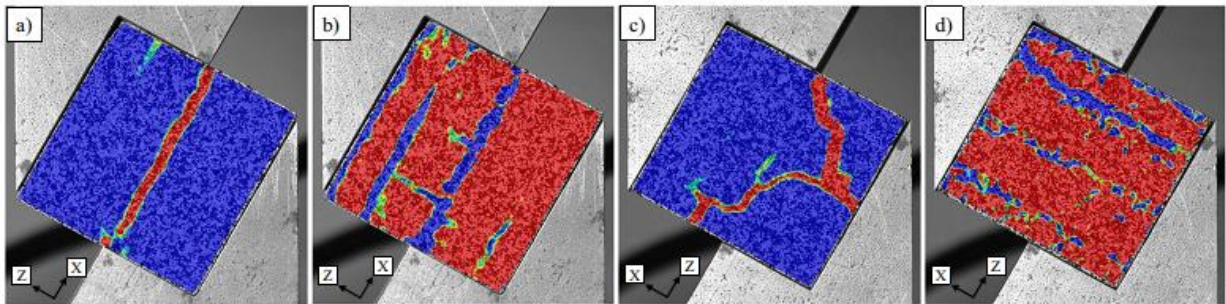
6.3.2. Oblique shear strength

The literature review did not find previous studies comparing the oblique shear strength between mold-cast and 3D-printed specimens. Similarly, no previous studies examined the

different loading directions of 3D-printed specimens. However, the present research showed a 48% strength reduction in the oblique shear test results of 3D-printed specimens when compared to standard mold-cast specimens, as shown in Table 6.3. Additionally, the ANOVA demonstrated an anisotropic behavior between the three loading directions of the 3D-printed specimens. Notably, the COV values for each specimen group remained within an acceptable range, varying from 0.1% to 6.4%, as shown in Table 6.3. These results highlight the potential of the oblique shear test as a simple and viable approach for assessing the shear strength of 3D-printed structures, which aligns with the assertion made by Mechtcherine *et al.* (2022).

The DIC results obtained from the current study showed a distribution of the minor strain within the interlayers of 3D-printed specimens, as illustrated in Figure 6.7. This behavior influenced the major strain behavior of 3D-printed specimens loaded in the Z-direction. However, this deviation was not strong enough to alter the final failure that occurred due to the fracture, which was parallel to the loading plane.

Figure 6.7 - DIC analysis of the 3D-printed specimens under oblique shear strength. a) principal major strain of cubes tested in X-direction; b) principal minor strain of cubes tested in X-direction; c) principal major strain of cubes tested in Z-direction; d) principal minor strain of cubes tested in Z-direction



Source: Author (2023)

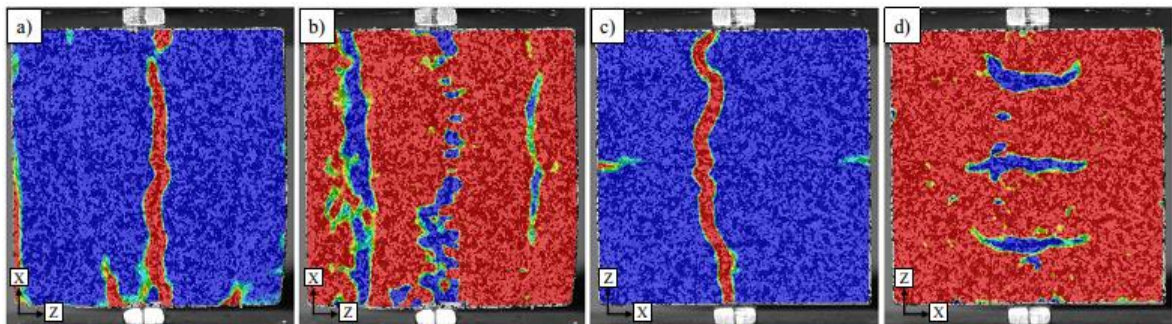
6.3.3. Splitting tensile strength

The splitting tensile strength tests conducted by (DING *et al.*, 2020; WOLFS; BOS; SALET, 2019) revealed average strength reductions from mold-cast to 3D-printed specimens of 26% and 11%, respectively. Whereas in the present research, this value corresponds to 45%, as described in Table 6.3. When comparing 3D-printed specimens tested in the X-direction, the splitting tensile test yielded comparable results (2.6 MPa) to the three and four-point flexural strength tests (2.6 and 2.7 MPa, respectively), as shown in Table 6.3.

Furthermore, the ANOVA of the splitting tensile test demonstrated isotropy in the 3D-printed specimens, which aligns with the findings reported in (WOLFS; BOS; SALET, 2019). However, both three and four-point flexural strength tests have shown anisotropic behavior based on the ANOVA. Prior studies (MECHTCHERINE et al., 2022) have highlighted that even the splitting tensile strength test conducted with cylinders can pose challenges in terms of simplicity and clarity when characterizing the anisotropic behavior of the 3D-printed specimens. This is attributed to the characteristics of the test setup, where the imposition of a fracture plane restricts the 3D-printed specimen from naturally attaining its ultimate tensile strength along its weakest plane, as typically observed in flexural strength tests.

The DIC analysis, depicted in Figure 6.8, confirmed that despite the distribution of minor strain within all the interlayers of the 3D-printed specimens, the major strain behavior and the fracture plane remained on the loading plane. Based on these findings, the splitting tensile strength test may not be the most suitable method for accurately evaluating the tensile strength or the interlayer bond strength of 3D-printed structures.

Figure 6.8 - DIC analysis of the 3D-printed specimens under splitting tensile strength. a) principal major strain of cubes tested in X-direction; b) principal minor strain of cubes tested in X-direction; c) principal major strain of cubes tested in Z-direction; d) principal minor strain of cubes tested in Z-direction



Source: Author (2023)

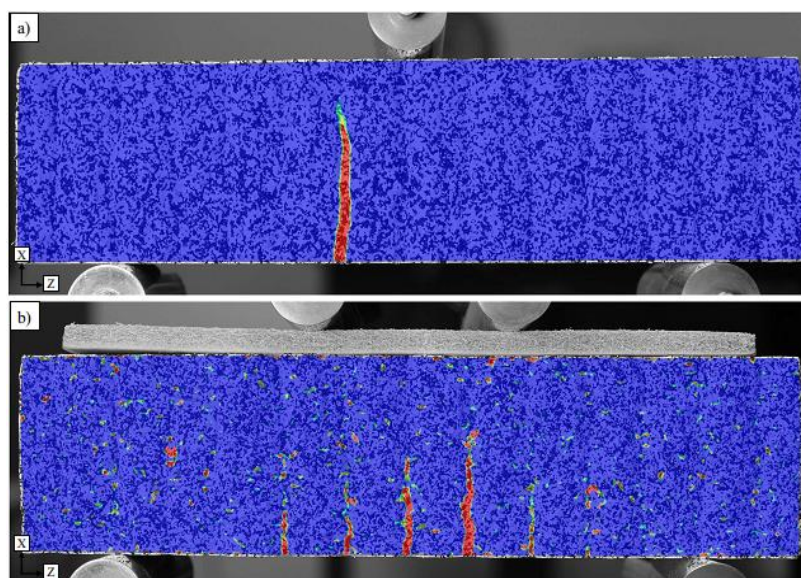
6.3.4. Three and four-point flexural strengths

The anisotropic behavior of 3D-printed specimens was evident in the three and four-point flexural strength tests. Notably, in both tests, the 3D-printed specimens tested in the X-direction yielded the lowest strength results among all specimens. These findings are consistent with flexural strength tests conducted by previous studies (DING et al., 2020; LE et al., 2012;

LIU et al., 2022a; MECHTCHERINE et al., 2019b; MEURER; CLASSEN, 2021; ÖZALP; YILMAZ, 2020; RAHUL et al., 2019; WOLFS; BOS; SALET, 2019; YU et al., 2021). These studies reported varying degrees of strength reduction between mold-cast and 3D-printed specimens tested in the X-direction, with the lowest being 14% [31,59] and the highest being 66% (MECHTCHERINE et al., 2019b). Whereas in the present research, these values corresponded to 54% and 51% in the three and four-point flexural strength tests, respectively (refer to Table 6.3).

It should be highlighted that the three-point flexural strength test exhibited higher COV values than the four-point flexural strength test, as shown in Table 6.3. Remarkably, the precision of the latter was so high that no adjustments related to precision and bias (ASTM INTERNATIONAL, 2021d) were necessary. Furthermore, the DIC analysis of the flexural strength tests revealed that the major strain developed vertically, and the fracture plane occurred solely in the interlayer regions. However, distinct differences were noted between them. In the three-point flexural strength test, the strain behavior was concentrated in one of the interlayers, close to the center of the specimen. While in the four-point flexural strength test, the strain was distributed among the lower region of multiple interlayers located within the upper span, where the maximum moment occurs. This discrepancy is highlighted in Figure 6.9.

Figure 6.9 - DIC analysis of the 3D-printed specimens under flexural strength. a) three-point flexural test, principal major strain of prisms tested in X-direction; b) four-point flexural test, principal major strain of prisms tested in X-direction



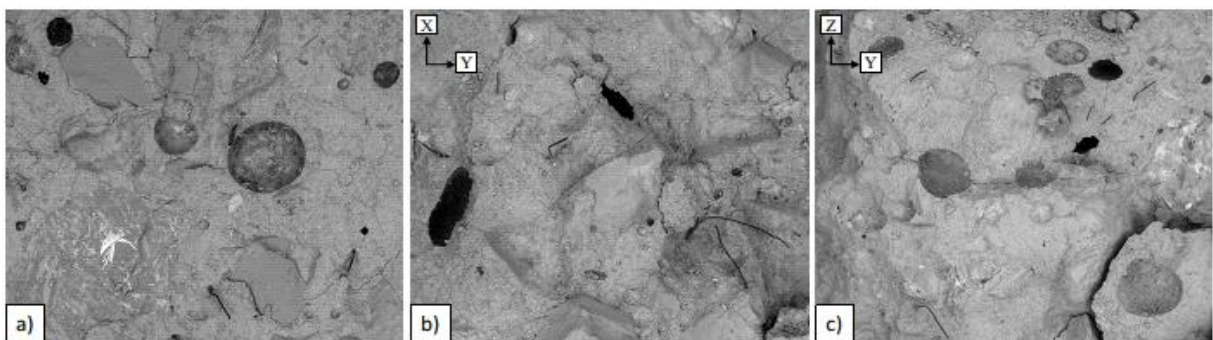
Source: Author (2023)

6.4. Microstructural tests

The SEM analysis unveiled notable differences in pore morphology between mold-cast and 3D-printed specimens. The pores in the mold-cast specimens appeared more spherical in shape. While in the 3D-printed specimens, the pores exhibited an elongated form in the XY plane, aligned with the printing direction (X-direction), and appeared flattened in the YZ plane, as shown in Figure 6.10. These findings are consistent with previous studies (HEEVER *et al.*, 2022; KRUGER; DU PLESSIS; VAN ZIJL, 2021; LIU *et al.*, 2022a; VAN DEN HEEVER *et al.*, 2022b; WU *et al.*, 2023; YU *et al.*, 2021).

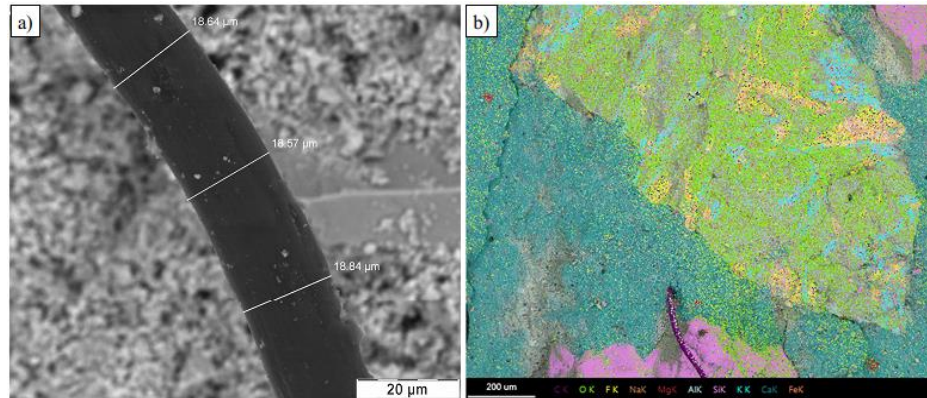
Moreover, the samples were analyzed for the presence of fibers, which were found to have an average diameter of 18.7 μm , as illustrated in Figure 6.11. Additionally, the EDS analysis indicated that they were mainly composed of carbon. Figure 6.11 illustrates the distribution of elements on the analyzed image. As previously noted by Mechtcherine *et al.* (2022), the presence of fibers can influence the material flow pattern, also leading to anisotropic behavior. However, it should be highlighted that the SEM analysis did not provide clear insights into the orientation of the fibers and how it could influence the anisotropy of 3D-printed specimens.

Figure 6.10 – Pore morphology. a) mold-cast sample at magnitude 35x; b) 3D-printed sample in XY plane at magnitude 35x; c) 3D-printed sample in YZ plane at magnitude 30x



Source: Author (2023)

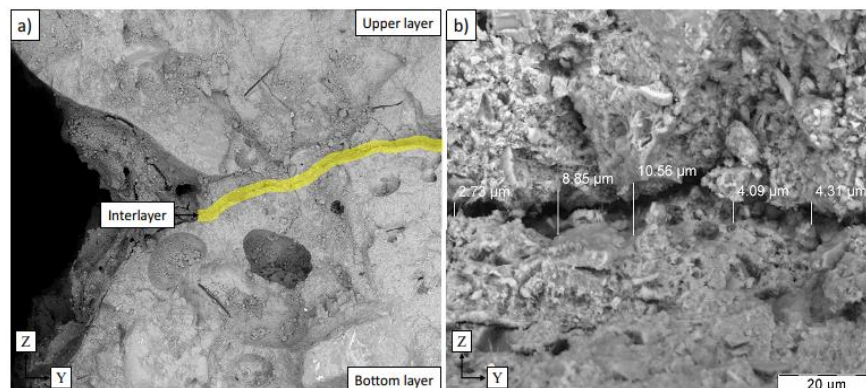
Figure 6.11 – SEM and EDS analyses on the fibers. a) fiber diameters recorded at magnitude 1500x; b) overlay of elements at magnitude 110x



Source: Author (2023)

Regarding the interlayer of 3D-printed specimens, the SEM analysis revealed a distinct visibility of the interlayer bond at the edges of the 3D-printed samples in the YZ plane, as shown in Figure 6.12. Nonetheless, as the analysis moved closer to the center of the samples, the visibility of the interlayer bond progressively decreased. This observation provides evidence that the layer time was sufficiently short to establish a cohesive bond between adjacent layers. These findings align with similar results reported by Kruger, du Plessis, and van Zijl (2021). Furthermore, these statements are also supported by the physical test results of the 3D-printed specimens, which demonstrated higher density and lower total void volume than the mold-cast specimens, as presented in Table 6.2. The SEM image unveiled that the visible portion of the interlayer bond exhibited an average width of 6.1 μm , as illustrated in Figure 6.12.

Figure 6.12 – SEM analysis on the interlayer at YZ plane. a) Visible portion of the interlayer at the edge of the 3D-printed sample, at magnitude 30x; b) Widths recorded at the visible portion of the interlayer, at magnitude 1500x



Source: Author (2023)

7. CONCLUSION

The primary objective of this study was to investigate the material properties of a 3D-printable structural mortar, focusing on a comparative analysis of physical, mechanical, and microstructural properties between 3D-printed and mold-cast specimens. The anisotropic nature and the strain behavior of the 3D-printed specimens were evaluated under different loading scenarios and directions. The main conclusions from this research can be summarized as follows:

- i. 3D-printed specimens exhibited a 0.5% higher average density and 6% lower total void volume compared to mold-cast specimens (Table 6.2). The use of short layer times during printing contributed to this achievement (Table 5.1). This finding is consistent with SEM analysis, which revealed an indiscernible interlayer bond at the center of the 3D-printed samples (section 6.4).
- ii. The SEM analysis revealed different pore morphology in mold-cast and 3D-printed specimens. While the mold-cast samples displayed more spherical pores, the 3D-printed samples exhibited pores elongated in the XY plane, mostly aligned with the printing direction (X-direction), and flattened in the YZ plane (Figure 6.10).
- iii. Across all mechanical tests, the 3D-printed specimens exhibited an average strength reduction of 43% when compared to the mold-cast specimens (Table 6.3). This outcome aligns with the UPV test results, indicating an average UPV 13% higher for mold-cast specimens than for 3D-printed ones (Table 6.2). The cause of this loss in strength lies in the uneven distribution of pores within 3D-printed specimens, particularly concentrated within the interlayers, resulting in weaker interfaces compared to the rest of the layer regions. Furthermore, this statement was confirmed by DIC analyses, revealing predominant strain propagation within the interlayers (section 6.3).

- iv. The 3D-printed specimens exhibited distinct anisotropic behavior under compressive strength (Table 6.3), a characteristic reinforced by the UPV test results (Table 6.2). Notably, the compressive strength test yielded low COV values for each specimen group, thus establishing its validity as an effective method for evaluating the compressive strength of 3D-printed components.
- v. The stress-strain curve obtained from the 3D-printed specimens in the Z-direction, which refers to the height of the wall, exhibited optimal suitability for characterizing the behavior of analogous 3D-printed structures under compressive strength (Figure 6.6, Equations 6.2, and 6.3). When compared to the mold-cast specimens, they exhibited a 31% reduction in stiffness, a 38% reduction in the ultimate stress, and a 10% reduction in strain (Table 6.4).
- vi. The oblique shear strength test exhibited clear anisotropy among 3D-printed specimens (Table 6.3). Particularly, the COV values for each specimen group remained within an acceptable range, varying from 0.1% to 6.4%. These findings emphasize the potential of the oblique shear test as a simple and viable option for assessing the shear strength of 3D-printed structures.
- vii. The interlayer bond strength was evaluated through three distinct tests: (iii.c) splitting tensile strength, (iii.d) three-point flexural strength, and (iii.e) four-point flexural strength (Table 5.3). The results revealed a false isotropic behavior of 3D-printed specimens in test iii.c, and a distinct anisotropic behavior in tests iii.d and iii.e (Table 6.3). Comparably, test iii.e exhibited the highest precision. Based on these findings, the four-point flexural strength test in X-direction was recommended as the preferred method for assessing the interlayer bond strength of 3D-printed structures.

7.1. Recommendations

The 3D printing of cementitious materials has demonstrated significant potential for automating civil construction processes. However, certain aspects require further investigation to fully understand and optimize the mechanical behavior of 3D-printed structures. Notably, additional research on the influence of fiber orientation on the mechanical behavior of 3D-printed specimens is suggested. Moreover, it is recommended to conduct further studies to validate the effectiveness of the oblique shear test method in assessing the shear strength of 3D-printed components along the X, Y, and Z directions. Finally, considering the recurring occurrence of cold joints in the 3D-printing process, it is crucial to explore the mechanical behavior of 3D-printed components with cold joints, along with cold joint reinforcement solutions.

REFERENCES

ADALOUDIS, M.; BONNIN ROCA, J. Sustainability tradeoffs in the adoption of 3D Concrete Printing in the construction industry. **Journal of Cleaner Production**, v. 307, n. February, p. 127201, 2021.

ANDREW, R. M. Global CO₂ emissions from cement production. **Earth System Science Data**, v. 10, p. 195–217, 2018.

ASTM INTERNATIONAL. C670 – 15: Standard Practice for Preparing Precision and Bias Statements for Test Methods for Construction Materials. Em: **Annual Book of ASTM Standards**. [s.l: s.n.]. v. 04.02p. 9.

ASTM INTERNATIONAL. C597-16: Standard Test Method for Pulse Velocity Through Concrete. Em: **Annual Book of ASTM Standards**. West Conshohocken: [s.n.]. v. 04.02p. 4.

ASTM INTERNATIONAL. C293/C293M-16: Standard Test Method for Flexural Strength of Concrete (Using Simple Beam with Center-Point Loading). Em: **Annual Book of ASTM Standards**. West Conshohocken: [s.n.]. v. 04.02p. 4.

ASTM INTERNATIONAL. C1723-16: Standard Guide for Examination of Hardened Concrete Using Scanning Electron Microscopy. Em: **Annual Book of ASTM Standards**. West Conshohocken: [s.n.]. v. 04.02p. 9.

ASTM INTERNATIONAL. C496/C496M-17: Standard Test Method for Splitting Tensile Strength of Cylindrical Concrete Specimens. Em: **Annual Book of ASTM Standards**. West Conshohocken: [s.n.]. v. 04.02p. 5.

ASTM INTERNATIONAL. C1437-20: Standard Test Method for Flow of Hydraulic Cement Mortar. Em: **Annual Book of ASTM Standards**. West Conshohocken: [s.n.]. v. 04.01p. 2.

ASTM INTERNATIONAL. C136/C136M-19: Standard Test Method for Sieve Analysis of Fine and Coarse Aggregates. Em: **Annual Book of ASTM Standards**. West Conshohocken: [s.n.]. v. 04.02p. 5.

ASTM INTERNATIONAL. E11-20: Standard Specification for Woven Wire Test Sieve Cloth and Test Sieves. Em: **Annual Book of ASTM Standards**. West Conshohocken: [s.n.]. v. 14.02p. 12.

ASTM INTERNATIONAL. C109/C109M-21: Standard test method for compressive strength of hydraulic cement mortars (Using 2-in. or cube specimens). Em: **Annual Book of ASTM Standards**. West Conshohocken: [s.n.]. v. 04.01p. 12.

ASTM INTERNATIONAL. C348-21: Standard Test Method for Flexural Strength of Hydraulic-Cement Mortars. Em: **Annual Book of ASTM Standards**. West Conshohocken: [s.n.]. v. 04.01p. 6.

ASTM INTERNATIONAL. C642-21: Standard Test Method for Density, Absorption, and Voids in Hardened Concrete. Em: **Annual Book of ASTM Standards**. West Conshohocken: [s.n.]. v. 04.02p. 3.

ASTM INTERNATIONAL. C78/C78M-21: Standard Test Method for Flexural Strength of Concrete (Using Simple Beam with Third-Point Loading). Em: **Annual Book of ASTM Standards**. West Conshohocken: [s.n.]. v. 04.02p. 5.

- BATIKHA, M. et al. 3D concrete printing for sustainable and economical construction: A comparative study. **Automation in Construction**, v. 134, n. November 2021, p. 104087, 2022.
- BOS, F. P. et al. Experimental exploration of metal cable as reinforcement in 3D printed concrete. **Materials**, v. 10, n. 1314, p. 22, 2017.
- BUSWELL, R. et al. Geometric quality assurance for 3D concrete printing and hybrid construction manufacturing using a standardised test part for benchmarking capability. **Cement and Concrete Research**, v. 156, n. April, p. 106773, 2022.
- BUSWELL, R. A. et al. Freeform Construction : Mega-scale Rapid Manufacturing for construction. **Automation in Construction**, v. 16, p. 224–231, 2007.
- CHEN, Y. et al. A review of printing strategies, sustainable cementitious materials and characterization methods in the context of extrusion-based 3D concrete printing. **Journal of Building Engineering**, v. 45, n. November 2021, 2022a.
- CHEN, Y. et al. Effect of curing methods during a long time gap between two printing sessions on the interlayer bonding of 3D printed cementitious materials. **Construction and Building Materials**, v. 332, 16 maio 2022b.
- CHO, S. et al. **Mechanical evaluation of 3D printable nano-silica incorporated fibre-reinforced lightweight foam concrete**. International Association for Fracture Mechanics of Concrete and Concrete Structures, 19 jun. 2019.
- DAUNGWILAILUK, T.; PHEINSUSOM, P.; PANSUK, W. Uniaxial load testing of large-scale 3D-printed concrete wall and finite-element model analysis. **Construction and Building Materials**, v. 275, p. 122039, 2021.
- DEMIRAL, N. C. et al. Mechanical anisotropy evaluation and bonding properties of 3D-printable construction and demolition waste-based geopolymer mortars. **Cement and Concrete Composites**, v. 134, 1 nov. 2022.
- DEPARTMENT OF DEFENSE. **Unified Facilities Criteria (UFC) 3-301-01**. Washington, D.C.: [s.n.].
- DING, T. et al. Hardened properties of layered 3D printed concrete with recycled sand. **Cement and Concrete Composites**, v. 113, n. February, p. 103724, 2020.
- EDISON, T. A. **US1219272A: Process of constructing concrete buildings**. United StatesUnited States Patent Office, , 13 mar. 1917.
- FARINA, I. et al. On the reinforcement of cement mortars through 3D printed polymeric and metallic fibers. **Composites Part B: Engineering**, v. 90, p. 76–85, 2016.
- FAST TRACK ACTION SUBCOMMITTEE ON CRITICAL AND EMERGING TECHNOLOGIES. **Critical and Emerging Technologies List Update**. Washington, D.C.: [s.n.].
- GEBHARD, L. et al. Structural behaviour of 3D printed concrete beams with various reinforcement strategies. **Engineering Structures**, v. 240, n. April, 2021.
- GOM. **GOM Correlate Pro: Strains and displacements from motion pictures**. Disponível em: <<https://www.gom.com/en/products/gom-suite/gom-correlate-pro>>. Acesso em: 2 maio. 2022.

- GOSSELIN, C. et al. Large-scale 3D printing of ultra-high performance concrete - a new processing route for architects and builders. **Materials and Design**, v. 100, p. 102–109, 2016.
- HAN, X. et al. Experimental study on large-scale 3D printed concrete walls under axial compression. **Automation in Construction**, v. 133, n. December 2020, p. 103993, 2022.
- HEEVER, M. VAN DEN et al. A mechanistic evaluation relating microstructural morphology to a modified Mohr-Griffith compression-shear constitutive model for 3D printed concrete. **Construction and Building Materials**, v. 325, n. February, p. 126743, 2022.
- HEIDARNEZHAD, F.; ZHANG, Q. Shotcrete based 3D concrete printing: State of art, challenges, and opportunities. **Construction and Building Materials**, v. 323, n. October 2021, p. 126545, 2022.
- HOJATI, M. et al. Barbed-wire reinforcement for 3D concrete printing. **Automation in Construction**, v. 141, 1 set. 2022.
- HOSSEINI, E. et al. A novel method to enhance the interlayer bonding of 3D printing concrete: An experimental and computational investigation. **Cement and Concrete Composites**, v. 99, n. March, p. 112–119, 2019.
- HOU, S. et al. Fresh properties of 3D printed mortar with recycled powder. **Construction and Building Materials**, v. 309, n. June, p. 125186, 2021.
- ISO/TC 261 ADDITIVE MANUFACTURING. **ISO/ASTM DIS 52939: Additive manufacturing for construction — Qualification principles — Structural and infrastructure elements**. [s.l.: s.n.]. Disponível em: <<https://www.iso.org/standard/81177.html>>. Acesso em: 14 jun. 2023.
- KEITA, E. et al. Weak bond strength between successive layers in extrusion-based additive manufacturing: measurement and physical origin. **Cement and Concrete Research**, v. 123, 1 set. 2019.
- KRUGER, J.; DU PLESSIS, A.; VAN ZIJL, G. An investigation into the porosity of extrusion-based 3D printed concrete. **Additive Manufacturing**, v. 37, 1 jan. 2021.
- KRUGER, J.; ZIJL, G. VAN. A compendious review on lack-of-fusion in digital concrete fabrication. **Additive Manufacturing**, v. 37, n. August 2020, p. 101654, 2021.
- LE, T. T. et al. Hardened properties of high-performance printing concrete. **Cement and Concrete Research**, v. 42, n. 3, p. 558–566, 2012.
- LIU, C. et al. Analysis of the mechanical performance and damage mechanism for 3D printed concrete based on pore structure. **Construction and Building Materials**, v. 314, 3 jan. 2022a.
- LIU, H. et al. 3D printing concrete with recycled coarse aggregates: The influence of pore structure on interlayer adhesion. **Cement and Concrete Composites**, v. 134, 1 nov. 2022b.
- LIU, X.; SUN, B. The influence of interface on the structural stability in 3D concrete printing processes. **Additive Manufacturing**, v. 48, n. PB, p. 102456, 2021.
- MECHTCHERINE, V. et al. Large-scale digital concrete construction – CONPrint3D concept for on-site, monolithic 3D-printing. **Automation in Construction**, v. 107, n. August, p. 102933, 2019a.
- MECHTCHERINE, V. et al. Large-scale digital concrete construction – CONPrint3D concept for on-site, monolithic 3D-printing. **Automation in Construction**, v. 107, 1 nov. 2019b.

- MECHTCHERINE, V. et al. A roadmap for quality control of hardening and hardened printed concrete. **Cement and Concrete Research**, v. 157, 1 jul. 2022.
- MEURER, M.; CLASSEN, M. Mechanical properties of hardened 3D printed concretes and mortars-development of a consistent experimental characterization strategy. **Materials**, v. 14, n. 4, p. 1–23, 2021.
- MOELICH, G. M.; KRUGER, J.; COMBRINCK, R. Modelling the interlayer bond strength of 3D printed concrete with surface moisture. **Cement and Concrete Research**, v. 150, n. May, p. 106559, 2021.
- MOHAN, M. K. et al. Extrusion-based concrete 3D printing from a material perspective: A state-of-the-art review. **Cement and Concrete Composites**, v. 115, n. October 2020, p. 103855, 2021.
- NEMATOLLAHI, B.; XIA, M.; SANJAYAN, J. Current progress of 3D concrete printing technologies. **ISARC 2017 - Proceedings of the 34th International Symposium on Automation and Robotics in Construction**, n. June, p. 260–267, 2017.
- NGUYEN-VAN, V. et al. 3D concrete printing modelling of thin-walled structures. **Structures**, v. 39, n. March, p. 496–511, 2022.
- ÖZALP, F.; YILMAZ, H. D. Fresh and Hardened Properties of 3D High-Strength Printing Concrete and Its Recent Applications. **Iranian Journal of Science and Technology - Transactions of Civil Engineering**, v. 44, p. 319–330, 1 out. 2020.
- PEGNA, J. Exploratory investigation of solid freeform construction. **Automation in Construction**, v. 5, n. 5, p. 427–437, 1997.
- RAHUL, A. V. et al. Mechanical characterization of 3D printable concrete. **Construction and Building Materials**, v. 227, 10 dez. 2019.
- REINOLD, J. et al. Extrusion process simulation and layer shape prediction during 3D-concrete-printing using the Particle Finite Element Method. **Automation in Construction**, v. 136, n. January, p. 104173, 2022.
- ROUSSEL, N. Rheological requirements for printable concretes. **Cement and Concrete Research**, v. 112, n. January, p. 76–85, 2018.
- SANJAYAN, J. G.; NAZARI, A.; NEMATOLLAHI, B. **3D Concrete Printing Technology**. [s.l.] Butterworth-Heinemann, 2019.
- SINGH, A. et al. Mechanical and macrostructural properties of 3D printed concrete dosed with steel fibers under different loading direction. **Construction and Building Materials**, v. 323, n. January, p. 126616, 2022.
- SKIBICKI, S. et al. The effect of using recycled PET aggregates on mechanical and durability properties of 3D printed mortar. **Construction and Building Materials**, v. 335, n. March, p. 127443, 2022.
- SOUZA, M. T. et al. 3D printed concrete for large-scale buildings: An overview of rheology, printing parameters, chemical admixtures, reinforcements, and economic and environmental prospects. **Journal of Building Engineering**, v. 32, n. February, 2020.

SUN, X. et al. Shear performance of 3D printed concrete reinforced with flexible or rigid materials based on direct shear test. **Journal of Building Engineering**, v. 48, n. December 2021, p. 103860, 2022.

TRAMONTIN SOUZA, M. et al. Role of chemical admixtures on 3D printed Portland cement: Assessing rheology and buildability. **Construction and Building Materials**, v. 314, n. November 2021, 2022.

TRAN, M. V.; CU, Y. T. H.; LE, C. V. H. Rheology and shrinkage of concrete using polypropylene fiber for 3D concrete printing. **Journal of Building Engineering**, v. 44, n. September, p. 103400, 2021.

VAN DEN HEEVER, M. et al. Numerical modelling strategies for reinforced 3D concrete printed elements. **Additive Manufacturing**, v. 50, n. March 2021, p. 102569, 2022a.

VAN DEN HEEVER, M. et al. Evaluating the effects of porosity on the mechanical properties of extrusion-based 3D printed concrete. **Cement and Concrete Research**, v. 153, 1 mar. 2022b.

VANTYGHM, G. et al. 3D printing of a post-tensioned concrete girder designed by topology optimization. **Automation in Construction**, v. 112, n. January, p. 103084, 2020.

WANG, H. et al. Bond shear performances and constitutive model of interfaces between vertical and horizontal filaments of 3D printed concrete. **Construction and Building Materials**, v. 316, n. November 2021, p. 125819, 2022.

WANG, L. et al. Interlayer reinforcement of 3D printed concrete by the in-process deposition of U-nails. **Cement and Concrete Research**, v. 148, n. June, p. 106535, 2021.

WENG, Y. et al. Synchronized concrete and bonding agent deposition system for interlayer bond strength enhancement in 3D concrete printing. **Automation in Construction**, v. 123, n. January, p. 103546, 2021.

WOLFS, R. J. M.; BOS, F. P.; SALET, T. A. M. Hardened properties of 3D printed concrete : The influence of process parameters on interlayer adhesion. **Cement and Concrete Research**, v. 119, n. January, p. 132–140, 2019.

WU, Y. et al. 3D printed concrete with recycled sand: Pore structures and triaxial compression properties. **Cement and Concrete Composites**, v. 139, 1 maio 2023.

XIAO, J. et al. Large-scale 3D printing concrete technology: Current status and future opportunities. **Cement and Concrete Composites**, v. 122, n. May, p. 104115, 2021.

XIAO, J. et al. Bending behaviour of steel cable reinforced 3D printed concrete in the direction perpendicular to the interfaces. **Cement and Concrete Composites**, v. 125, n. April 2021, p. 104313, 2022.

XIAO, J.; LIU, H.; DING, T. Finite element analysis on the anisotropic behavior of 3D printed concrete under compression and flexure. **Additive Manufacturing**, v. 39, 1 mar. 2021.

XU, Y. et al. Correlation of interlayer properties and rheological behaviors of 3DPC with various printing time intervals. **Additive Manufacturing**, v. 47, n. April, p. 102327, 2021.

YANG, Y. et al. 3D-printing ultra-high performance fiber-reinforced concrete under triaxial confining loads. **Additive Manufacturing**, v. 50, n. September 2021, p. 102568, 2022a.

YANG, Y. et al. Mechanical anisotropy of ultra-high performance fibre-reinforced concrete for 3D printing. **Cement and Concrete Composites**, v. 125, 1 jan. 2022b.

YAO, H. et al. The relationship between the rheological behavior and interlayer bonding properties of 3D printing cementitious materials with the addition of attapulgite. **Construction and Building Materials**, v. 316, n. November 2021, p. 125809, 2022.

YU, S. et al. Microstructural characterization of 3D printed concrete. **Journal of Building Engineering**, v. 44, 1 dez. 2021.

ZHANG, H.; XIAO, J. Plastic shrinkage and cracking of 3D printed mortar with recycled sand. **Construction and Building Materials**, v. 302, n. July, p. 124405, 2021.